

1 **Blowing snow contributions to the Arctic snow-on-sea ice**
2 **budget using ICESat-2 observations**

3
4 Joseph Robinson¹, Lyatt Jaeglé¹, Stephen P. Palm^{2,3}, Glen E. Liston⁴

5
6 ¹ Department of Atmospheric and Climate Science, University of Washington, Seattle, WA, USA

7 ² Science Systems and Applications, Lanham, MD, USA

8 ³ NASA Goddard Space Flight Center, Greenbelt, MD, USA

9 ⁴ Cooperative Institute for Research in the Atmosphere (CIRA), Colorado State University, Fort Collins, CO, USA

10
11 *Correspondence to:* Joseph Robinson (jrobin15@uw.edu)

47 **Abstract**

48
49 Blowing snow modulates the evolution of snow over Arctic sea ice through redistribution and
50 sublimation. Here, we present the first multi-year pan-Arctic observational estimates of blowing
51 snow occurrence, properties, and associated fluxes based on NASA Ice, Cloud and land
52 Elevation Satellite 2 (ICESat-2) satellite observations for five cold seasons (November through
53 April 2018-2023). On average, ICESat-2 detects blowing snow 19% of the time over sea ice,
54 with localized frequencies reaching up to 35% in the Central Arctic, where blowing snow heights
55 (optical depths) reach 150 m (0.20). We find that blowing snow occurrence shows strong
56 interannual variability related to large-scale climate variability, particularly the Arctic Oscillation
57 (AO). During positive AO phases, blowing snow occurrence increases substantially, with up to a
58 two-fold increase in the Central Arctic. Blowing snow occurrence, height, and optical depth all
59 exhibit a strong dependence on wind speed, increasing by more than five-fold between 4 and 15
60 m s^{-1} . ICESat-2 blowing snow sublimation estimates average 1.63 cm snow-water-equivalent
61 (SWE) per cold season, thus removing 14% of pan-Arctic snowfall. In the Central Arctic, the
62 offset is 18-24%. These values are consistent with simulations from the high-resolution
63 SnowModel-LG (1.66 cm SWE) and a simpler, threshold-based model (2.07 cm SWE).
64 Interannual variability in snowfall and sublimation can be 1-2 cm SWE, though not always in
65 phase, resulting in snowfall removals that range from 9% to 20%. Critically, these findings
66 provide satellite-based constraints on blowing snow processes over sea ice and underscore the
67 importance of blowing snow sublimation in the Arctic snow budget.

68 69 **1 Introduction**

70
71 Snow cover on sea ice is a fundamental component of the Arctic climate system, influencing
72 surface albedo, insulating the ocean from the atmosphere, and modulating the exchange of heat
73 and moisture across the ocean-ice-atmosphere interface (Merkouriadi, Cheng, et al., 2017;
74 Merkouriadi, Gallet, et al., 2017; Sturm et al., 2002; Webster et al., 2018). Its presence impacts
75 not only the local energy balance but also broader climate feedbacks that affect both high- and
76 mid-latitudes. As the Arctic undergoes rapid environmental change, including thinning sea ice
77 (Kwok & Untersteiner, 2011; Stroeve & Notz, 2018), shifting precipitation patterns (Bintanja,
78 2018; Bintanja & Andry, 2017; McCrystall et al., 2021), and increasing temperatures (Rantanen
79 et al., 2022), the need to accurately characterize the spatial and temporal variability of snow on
80 sea ice has become increasingly urgent. Understanding how the snowpack and its properties
81 evolve across a range of spatial and temporal scales and in response to dynamic atmospheric
82 processes is essential for improving predictions of sea ice behavior, refining climate model
83 simulations, and assessing implications for Arctic ecosystems, human activities, and global
84 climate.

85
86 While the snowpack on sea ice generally follows a seasonal cycle of winter accumulation and
87 summer melt, shorter-term processes can alter characteristics and accumulation rates. One such
88 process is blowing snow, which occurs when strong winds lift snow away from the surface.
89 Numerous studies spanning several decades have underscored the role of blowing snow in
90 modulating sea and land ice mass balance (Déry & Yau, 2002; Gallée et al., 2001; Palm et al.,
91 2017), altering radiative properties in polar regions (Lesins et al., 2009; Y. Yang et al., 2014),
92 impacting chemical processes in the polar troposphere (Frey et al., 2020; Gong et al., 2023;

93 Huang et al., 2020; Huang & Jaeglé, 2017; Krnavek et al., 2012; X. Yang et al., 2008), and
94 complicating the interpretation of physical and chemical ice core records (King et al., 2004;
95 Rhodes et al., 2017). Yet, capturing the full spatial and temporal variability of blowing snow
96 remains challenging due to the limited availability of sustained, regionally comprehensive
97 observations (Déry & Yau, 2001; Mann et al., 2000; Nishimura & Nemoto, 2005).

98
99 When lifted into the air, blowing snow particles are exposed to conditions that can promote their
100 sublimation, making blowing snow sublimation a significant pathway for both snow removal and
101 a source of atmospheric moisture. While sublimation can occur directly at the snow surface, it is
102 far more efficient when particles are suspended aloft, where their full surface area interacts with
103 the ambient air (Liston & Sturm, 2004; Schmidt, 1982). In addition, fragmentation within the
104 saltation layer may generate smaller particles that are readily suspended, increasing mass flux
105 and further enhancing sublimation rates (Huang et al., 2025). Model-based assessments suggest a
106 substantial role for blowing snow sublimation in the Arctic hydrological cycle: J. Yang et al.
107 (2010) estimated that over 27% of winter snowfall poleward of 70°N may be lost to blowing
108 snow sublimation. However, other modeling studies (e.g., Chung et al., 2011; Déry & Yau,
109 2002) have reported much lower estimates (6-7%), underscoring the considerable uncertainty
110 that still surrounds blowing snow related processes. Narrowing these uncertainties and
111 understanding the implications of sublimation-driven snow loss over sea ice remains a pressing
112 scientific challenge.

113
114 The time evolution of snow-water-equivalent (SWE) depth can be described by the mass balance
115 equation:

$$116 \quad \frac{dSWE}{dt} = \frac{1}{\rho_w} [P - (M + Q_{ss} + Q_{bs}) + Q_t] \quad (1)$$

117
118 where ρ_w is the density of water, and the terms represent inputs from precipitation (P ; $\text{kg m}^{-2} \text{s}^{-1}$)
119 and losses via melt (M , $\text{kg m}^{-2} \text{s}^{-1}$) and sublimation ($\text{kg m}^{-2} \text{s}^{-1}$), either from a static, non-blowing
120 snow surface (Q_{ss}) or via blowing snow (Q_{bs}). Erosion and deposition by blowing snow transport
121 (Q_t , $\text{kg m}^{-2} \text{s}^{-1}$) can also play a role in shaping the local snowpack. While Eq. 1 represents key
122 drivers of snowpack evolution, other processes, such as ice dynamics (e.g., creation and
123 destruction of parcels through ice motion, divergence, and convergence), may also play
124 important roles.

125
126 Efforts to quantify the influence of blowing snow on SWE often rely on empirical
127 parameterizations of snow transport and sublimation derived from sparse observations. These
128 approaches typically use meteorological inputs such as windspeed, air temperature, and snow age
129 to estimate thresholds for blowing snow initiation and subsequent sublimation (e.g., Gallée et al.,
130 2001, 2013; Lenaerts et al., 2010, 2012). In the Northern Hemisphere, model development has
131 primarily focused on continental snowpacks (Déry & Yau, 2001, 2002; Pomeroy et al., 1997; J.
132 Yang & Yau, 2007), where snow redistribution is critical to understand human relevant
133 hydrology and impacts to infrastructure. Although several studies have extended these
134 approaches to sea ice environments (Chung et al., 2011; Déry & Tremblay, 2004; Lecomte et al.,
135 2015; Liston et al., 2018, 2020; J. Yang et al., 2010), there remains a lack of direct, observation-
136 based constraints on pan-Arctic blowing snow processes over sea ice.

139 Spaceborne lidars offer a powerful means to address observational gaps and assess the
140 occurrence and impacts of blowing snow across large spatial and temporal domains. Palm et al.
141 (2011, 2017, 2018) developed a detection algorithm for the Cloud-Aerosol Lidar with
142 Orthogonal Polarization (CALIOP) aboard NASA’s CALIPSO satellite (Winker et al., 2009),
143 demonstrating that lidar backscatter measurements can be used to quantify key blowing snow
144 characteristics over Antarctica, including frequency of occurrence, height, optical depth, and
145 associated transport and sublimation fluxes. Building on this approach, a similar algorithm was
146 later adapted for the NASA Ice, Cloud, and land Elevation Satellite-2 (ICESat-2; Markus et al.,
147 2017) by Palm et al. (2021) and Herzfeld et al. (2021). Both algorithms were tailored to detect
148 blowing snow over the Antarctic continent. More recently, Robinson et al. (2025) optimized the
149 ICESat-2 blowing snow detection algorithm for application over Arctic sea ice, where more
150 frequent low-level cloud cover (Shupe et al., 2011; Zhang et al., 2019) increases the likelihood of
151 both false positives (i.e., clouds misidentified as blowing snow) and false negatives (i.e., blowing
152 snow misclassified as clear air) in lidar retrievals. Robinson et al. (2025) demonstrated that
153 retrieval errors caused by cloud interference can be effectively corrected, enabling the
154 development of a space-based blowing snow detection product specifically adapted for Arctic
155 sea ice.

156
157 In this study, our goal is to examine blowing snow occurrence and properties inferred from
158 ICESat-2 over Arctic sea ice across five cold seasons (defined as November through April)
159 between 2018 to 2023. We use ICESat-2 observations to infer blowing snow sublimation and its
160 role in the snow-on-sea ice budget. We compare the ICESat-2 observations to blowing snow
161 simulations from two models of varying complexity: a parameterization based on the PIEKTUK
162 blowing snow model (DY2001; Déry & Yau, 1999, 2001; J. Yang & Yau, 2007) and the state-of-
163 the-art Lagrangian snow-evolution model SnowModel-LG (Liston et al., 2020).

164
165 In Section 2 we provide details on the ICESat-2 blowing snow retrievals and inferred blowing
166 snow properties, SnowModel-LG predictions, and the DY2001 blowing snow sublimation
167 formulation. In Section 3 we present the ICESat-2 multi-year blowing snow occurrence
168 frequency and properties, examining key drivers of their spatiotemporal distribution. The role of
169 blowing snow in the snow-on-sea-ice budget is examined in Section 4 and conclusions are
170 presented in Section 5.

171

172 **2 Datasets and Methods**

173 **2.1 Satellite blowing snow retrievals from ICESat-2**

174

175 ICESat-2 was launched in 2018 in a precessing orbit with an altitude of ~ 500 km and inclination
176 of 92° , which allows for measurements up to 88° N latitude with a 91-day orbital repeat cycle
177 (Markus et al., 2017). ICESat-2 carries the Advanced Topographic Laser Altimeter System
178 (ATLAS), which is a single wavelength (532 nm), high repetition rate (10 kHz) lidar system with
179 photon counting detectors (Markus et al., 2017; Neumann et al., 2019). Each ATLAS laser pulse
180 is split into 3 simultaneous beam pairs (one strong and one weak beam per pair) by a diffractive
181 optical element. The 3 beam pairs are separated by about 3 km across track. Atmospheric
182 backscatter is obtained by ATLAS using only the three strong beams, spanning from the surface
183 to an altitude of 14 km, with an along-track resolution of approximately 280 m and a vertical
184 resolution of 30 m. Each 280 m ICESat-2 atmospheric profile represents the aggregate of 400

185 individual ATLAS laser shots (Palm et al., 2021). In this study we use ICESat-2 strong beam 1
186 observations from version 6 of the ATLAS/ICESat-2 Level 3A (ATL09) calibrated backscatter
187 profile product (Palm et al., 2023).
188

189 The algorithm used to detect blowing snow in ATLAS backscatter profiles is adapted from the
190 CALIOP approach (Palm et al., 2011) and further detailed in Palm et al. (2021; 2022). When a
191 surface return is identified and the 10 m wind speed from NASA’s GEOS-5 FP-IT analysis
192 exceeds 4 m s^{-1} , the algorithm compares the near-surface atmospheric backscatter to the expected
193 molecular (Rayleigh) signal. If the observed signal exceeds a fixed multiple of the molecular
194 scattering, the algorithm steps upward through each vertical bin until the backscatter drops below
195 an adaptive threshold (typically $\sim 2 \times 10^{-5} \text{ m}^{-1} \text{ sr}^{-1}$). To be flagged as blowing snow, the detected
196 feature must touch the ground and be shallower than 500 m. Retrievals deeper than 500m are
197 classified as diamond dust, which can stretch for a km or more vertically and frequently reaches
198 the ground (Intrieri & Shupe, 2004). Further, we use the version of the blowing snow algorithm
199 described in Robinson et al. (2025) which includes modifications to help alleviate several
200 challenges unique to the Arctic. These modifications serve to 1) minimize the misidentification
201 of low clouds as blowing snow and 2) correct for the attenuation due to transmissive clouds.
202

203 Once blowing snow is retrieved, its properties (geometric and optical depths) are logged. Optical
204 depth (OD) is estimated as the sum of the backscatter within the blowing snow retrieval
205 multiplied by the product of the bin depth (30 m) and the extinction to backscatter (lidar) ratio. A
206 lidar ratio of 25 sr is used, which is a typical value for ice crystals in cirrus clouds (Chen et al.,
207 2002; Josset et al., 2012). To infer blowing snow particle number density, transport flux, and
208 sublimation flux from the observed ICESat-2 backscatter we follow the same approach as
209 described in Palm et al. (2017) and Robinson et al. (2025), which relies on meteorological fields
210 (10 m wind speed, 2 m temperature, and 2 m relative humidity over ice) from the NASA GEOS-
211 5 FP-IT analysis (run at 0.5° latitude \times 0.625° longitude; Lucchesi et al., 2015) as well as
212 assumptions about blowing snow particle size. As in Robinson et al. (2025) we use the
213 formulation $r(z) = 5.05 \times 10^{-5} z^{-0.085}$ to estimate the particle radius (r , meters) as a function of
214 altitude (z , meters). This fit was constrained by observations of blowing snow particle sizes
215 during the 2019-2020 Multidisciplinary drifting Observatory for the Study of Arctic Climate
216 (MOSAIC) campaign.
217

218 To improve signal-to-noise in sunlit conditions, we apply along-track averaging to the ICESat-2
219 observations when the solar elevation angle exceeds -7° , a threshold beyond which background
220 solar photons begin to significantly degrade sensitivity. Under these conditions, which affect late
221 February through April (Fig. S1), increased solar background can reduce the detectability of low-
222 backscatter features such as blowing snow. To mitigate this, we average the native 25 Hz (280
223 m) profiles to 1 Hz (~ 7 km) resolution, effectively reducing solar background noise and
224 enhancing the reliability of blowing snow retrievals. While this approach lowers spatial
225 resolution, it reduces false positive detections and provides a more robust estimate of blowing
226 snow properties under marginal lighting conditions without introducing significant biases in
227 seasonal statistics.
228

229 **2.2 Blowing snow model simulations from SnowModel-LG**

230

231 SnowModel-LG is a physics-based snow-on-sea ice model forced by atmospheric inputs of air
232 temperature, RH, winds, and precipitation by the NASA Modern-Era Retrospective analysis for
233 Research and Applications, version 2 (MERRA-2; Gelaro et al., 2017) as well as sea ice inputs
234 of concentration and parcel motion (Tschudi et al., 2019, 2020). At each 3-hour timestep,
235 SnowModel-LG performs mass-budget calculations (e.g., Eq. 1) where SWE depth evolution is
236 accounted for by snow gains, losses, and sea ice dynamics (Liston et al., 2020).

237
238 The MicroMet module (Liston & Elder, 2006) is used to time average (1-hourly to 3-hourly) and
239 distribute the MERRA-2 fields (0.5° latitude \times 0.625° longitude) to the sea ice parcels. As part of
240 this procedure, the MERRA-2 water equivalent precipitation is bias corrected (as described in
241 section 2.5 and Table 1 of Liston et al., (2020)) and partitioned into snowfall and rainfall based
242 on environmental conditions (Dai, 2008).

243
244 Blowing snow in SnowModel-LG is accounted for by SnowTran-3D (Liston et al., 2007, 2018;
245 Liston & Sturm, 1998). The snow threshold friction velocity, u_{*t} , is calculated as a function of
246 snow density, ρ_s , which is related to snow strength and hardness. Snow density evolution
247 includes the history of temperature, precipitation, and wind-transport. When the friction velocity
248 exceeds the threshold value, snow begins to be lifted off the surface, first into the saltation layer
249 (several cm thick) and then into the turbulent suspension layer (several m thick). The vertical
250 mass concentration in the blowing snow profile is estimated following Liston & Sturm (1998)
251 and is combined with the environmental conditions to calculate transport and sublimation fluxes.
252 Mass transport is related to the windspeed and vertical mass concentration. SnowModel-LG's
253 blowing snow sublimation is calculated as a function of several factors, including the vertical
254 mass concentration, temperature-dependent humidity gradients between the snow particles and
255 the atmosphere, conductive and advective energy- and moisture-transfer mechanisms, particle
256 size, and solar radiation. The SnowModel-LG blowing snow transport and sublimation fluxes
257 represent column integrated values in units of $\text{kg m}^{-1} \text{s}^{-1}$ and cm SWE d^{-1} , respectively.
258 SnowModel-LG variables are output as 3-hourly values on an EASE grid with a resolution of 25
259 km.

261 **2.3 Blowing snow sublimation estimates from DY2001**

262
263 We also include estimates of the bulk blowing snow sublimation rate (Q_{bs} in Eq. 1) using the
264 approach described by Déry & Yau (1999, 2001) and subsequently J. Yang & Yau (2007).
265 Throughout the analysis we refer to this approach as DY2001. We chose to include it because it
266 is computationally efficient and has been widely applied in studies of blowing snow aerosol
267 production over sea ice (e.g., Gong et al., 2023; Frey et al., 2020; Huang et al., 2020; Huang &
268 Jaeglé, 2017; X. Yang et al., 2008, 2019). Sublimation depends on several factors including
269 surface windspeed, temperature, and humidity deficit.

270
271 Following X. Yang et al. (2008), sublimation is scaled by snow age A' which accounts for the
272 reduced ease of wind lofting as snow ages. For a full description of the sublimation calculation
273 used here, we refer the reader to section 2.1.1 of X. Yang et al. (2008). In our calculations, we
274 adopt a representative mean snow age of 3 days over Arctic sea ice (Huang & Jaeglé, 2017).

275

276 A key factor controlling blowing snow occurrence in DY2001 is the threshold windspeed, which
277 follows Li & Pomeroy (1997a). The threshold windspeed ($U_t = 6.975 + 0.0033[T_{2m} + 27.27]^2$) is
278 estimated from the 2 m surface air temperature (T_{2m}) and has a minimum value of $\sim 7 \text{ m s}^{-1}$ at an
279 air temperature of -27°C . At both higher and lower temperatures, the threshold wind speed will
280 be larger (maximizing at $\sim 10 \text{ m s}^{-1}$ for temperatures near 0°C). We estimate the DY2001
281 threshold windspeed and blowing snow sublimation using the same meteorology (10 m
282 windspeed, 2 m temperature, and 2 m RH_{ice}) used to derive the ICESat-2 sublimation.
283

284 **2.4 ICESat-2 and model gridding procedure**

285
286 We aggregate the ICESat-2 observations to a National Snow and Ice Data Center (NSIDC)
287 Equal-Area Scalable Earth (EASE) grid (Brodzik & Knowles, 2002) with a horizontal resolution
288 of 100 km. This resolution balances spatial detail with observational coverage, ensuring
289 sufficient ICESat-2 sampling within each grid cell while minimizing noise that would arise at
290 finer resolutions due to the narrow swath of the lidar. Temporal resolution is determined by the
291 duration of the binning period, allowing flexibility to examine daily, seasonal, or multi-year
292 patterns.
293

294 Within each 100 km grid cell, the ICESat-2 blowing snow occurrence for a specified time
295 window is computed as the number of profiles with a blowing snow detection divided by the
296 total number of valid profiles. A valid profile is defined as one where the surface return is clearly
297 detected, which excludes profiles with optically thick cloud cover (optical depth > 3), where
298 surface detection is unreliable or is not achieved. For blowing snow properties such as geometric
299 and optical depths, only blowing snow retrievals are gridded.
300

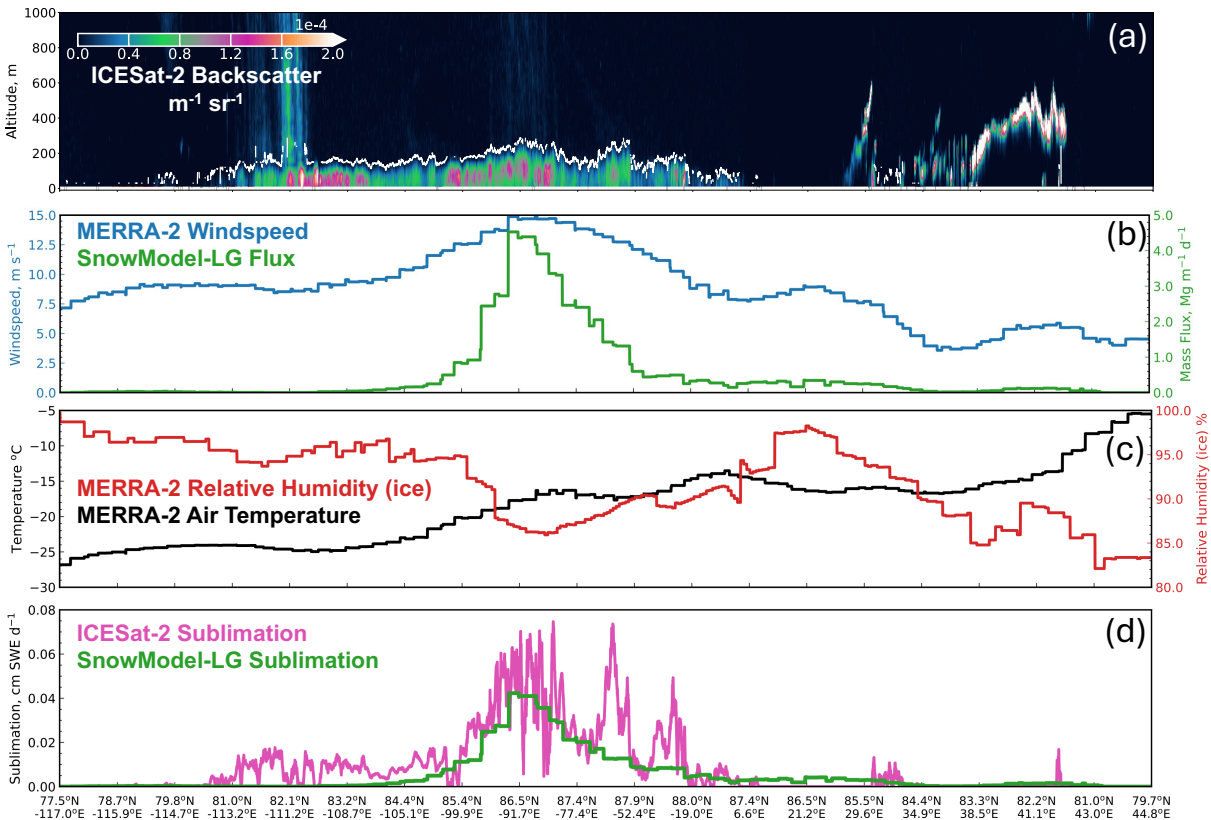
301 For comparison with model estimates, we extract values from the SnowModel-LG fields (25 km
302 resolution) by sampling the nearest-neighbor grid point to each valid ICESat-2 profile location.
303 These sampled values are then binned to the same 100 km EASE grid alongside the ICESat-2
304 data. We apply the same procedure to the DY2001 estimates: values are first computed at the
305 location of each valid ICESat-2 profile, and the resulting fields are aggregated onto the 100 km
306 grid for direct comparison with both ICESat-2 observations and SnowModel-LG outputs.
307

308 **2.5 December 2022 example of observed and predicted blowing snow**

309
310 Figure 1 highlights a blowing snow storm which occurred over the Central Arctic on 10
311 December 2022. During an orbit which transited from the Canadian Arctic Archipelago towards
312 Svalbard, ICESat-2 retrieved blowing snow for roughly 1,200 km along track, with depths up to
313 250 m and observed attenuated backscatter exceeding $1.50 \times 10^{-4} \text{ m}^{-1} \text{ sr}^{-1}$ (Fig. 1a). In this region,
314 MERRA-2 windspeeds ranged from 7.5 to 15 m s^{-1} (blue line, Fig. 1b) and SnowModel-LG
315 predicted intense blowing snow, with mass fluxes peaking at $4 \text{ Mg m}^{-1} \text{ d}^{-1}$ (green line, Fig. 1b).
316 The strongest ICESat-2 observed and SnowModel-LG predicted blowing snow occurred
317 coincident with the strongest winds (middle of Fig. 1a,b). While ICESat-2 did retrieve blowing
318 snow to the west of this maximum (left side, Fig. 1a) coincident with windspeeds $> 8 \text{ m s}^{-1}$,
319 SnowModel-LG predicted only minimal blowing snow mass transport.
320

321 At the location of intense blowing snow, MERRA-2 air temperatures ranged from -25°C to -15°C
 322 (black line, Fig. 1c) and the air was subsaturated with respect to ice (85-95%; red line, Fig. 1c).
 323 This combination of meteorological factors resulted in substantial blowing snow sublimation
 324 inferred from ICESat-2 and predicted by SnowModel-LG (Fig. 1d). ICESat-2 sublimation
 325 maximized at $0.07\text{ cm SWE d}^{-1}$ coincident with the strongest winds and driest conditions
 326 (magenta line, Fig. 1d). In the same region SnowModel-LG sublimation reached 0.05 cm SWE
 327 d^{-1} (green line, Fig. 1d).
 328

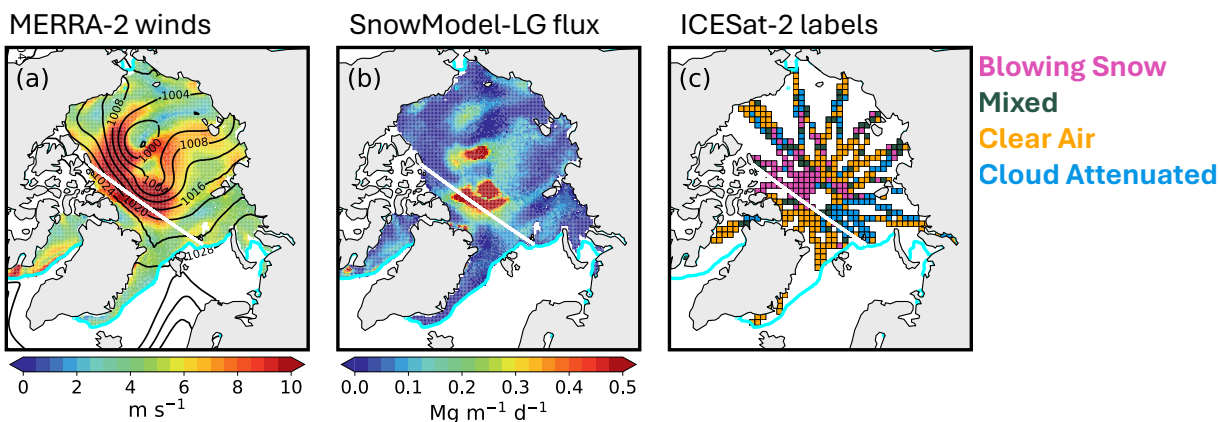
Blowing Snow Case: 10 December 2022



329 **Figure 1.** Case study of a blowing snow event in the Central Arctic on 10 December 2022. **(a)** ICESat-2 attenuated
 330 backscatter (shading, units $\text{m}^{-1}\text{ sr}^{-1}$) along an orbit from the Canadian Arctic Archipelago towards north of Svalbard.
 331 The white line indicates the top of the blowing snow layer. **(b)** MERRA-2 windspeed (blue line, units m s^{-1}) and
 332 SnowModel-LG blowing snow mass transport (green line, units $\text{Mg m}^{-1}\text{ d}^{-1}$) along the ICESat-2 orbit shown in panel
 333 a. **(c)** Near-surface MERRA-2 air temperature (black line, units $^{\circ}\text{C}$) and relative humidity over ice (red line, units %)
 334 along the ICESat-2 orbit shown in panel a. **(d)** Blowing snow sublimation (units cm SWE d^{-1}) inferred from ICESat-
 335 2 (magenta line) and predicted by SnowModel-LG (green line) along the ICESat-2 orbit shown in panel a. To reduce
 336 noise, the ICESat-2 sublimation has been averaged with a moving 8 km along-track window.
 337
 338
 339

340 Winds in excess of 8 m s^{-1} covered much of the Central Arctic and coincided with tight sea-level
 341 pressure (SLP) gradients stretching from the Beaufort to Lincoln Sea (Fig. 2a). SnowModel-LG
 342 predicted blowing snow mass transport $> 0.20\text{ Mg m}^{-1}\text{ d}^{-1}$ over an area of $750,000\text{ km}^2$ (Fig. 2b),
 343 which is slightly larger in size than the state of Texas. Given a total Central Arctic area of
 344 roughly 3.2 million km^2 , this storm impacted about a quarter of the basin.
 345

346 To examine the spatial distribution of ICESat-2 profiles, we first gridded the ICESat-2 orbits to
 347 the 100 km grid (Section 2.4) and then assigned each grid cell to one of four categories: blowing
 348 snow, mixed, clear air, or cloud attenuated. If more than 70% of all profiles were attenuated due
 349 to clouds, the grid cell was labeled as cloud attenuated. We assigned the other three categories
 350 based on the occurrence of blowing snow: blowing snow if more than 50% of profiles were
 351 blowing snow, mixed if 15-50% of profiles were blowing snow, and clear air if less than 15% of
 352 profiles were blowing snow. ICESat-2 grid cells in the western Central Arctic were consistently
 353 classified as blowing snow (magenta colors, Fig. 2c), coinciding with the strongest winds and the
 354 highest SnowModel-LG predicted transport. The total area of ICESat-2 grid cells labeled as
 355 blowing snow was 740,000 km², closely matching the SnowModel-LG predictions and
 356 confirming that the blowing snow was synoptic in scale, covering much of the Central Arctic.
 357



358 **Figure 2.** Arctic-wide spatial structure of the 10 December 2022 blowing snow event. (a) Spatial distribution of
 359 MERRA-2 windspeed (shading, units m s⁻¹) with sea-level pressure contours (black, 4 hPa intervals). (b) Spatial
 360 distribution of SnowModel-LG blowing snow mass transport (shading, units Mg m⁻¹ d⁻¹). (c) ICESat-2
 361 classifications at 100 km resolution: blowing snow (magenta), mixed (green), clear air (orange), or cloud attenuated
 362 (blue) as described in Section 2.5. In panels a-c, the cyan line marks the 15% sea ice contour, while the white line
 363 shows the track of ICESat-2 from Figure 1a.
 364

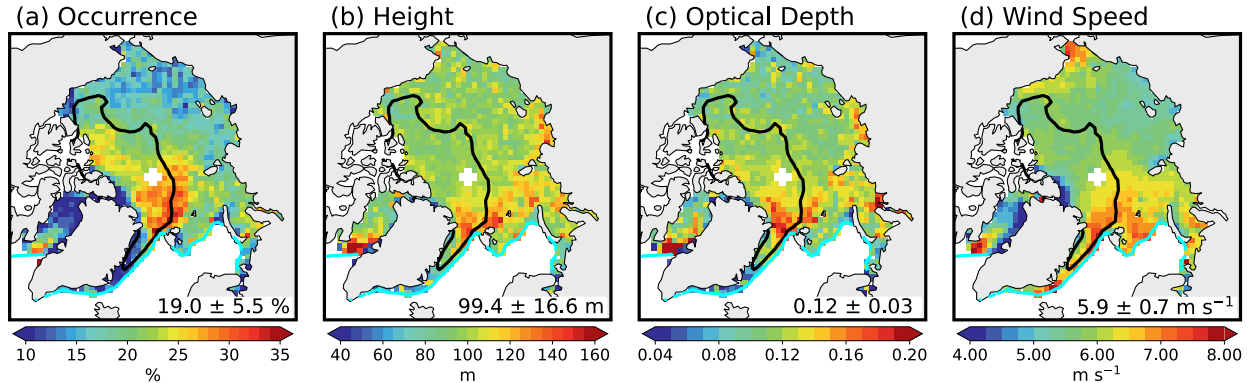
366 3 Blowing snow occurrence frequency and properties from ICESat-2

367 3.1 Spatiotemporal variability and drivers of blowing snow occurrence

368
 369 Figure 3 shows the mean multi-year blowing snow occurrence and properties derived from the
 370 ICESat-2 observations for November through April 2018-2023. To generate the average maps,
 371 we grid each cold season independently (following Section 2.4) and then average the five cold
 372 seasons together. We found a significant fraction of the central Arctic experiences blowing snow
 373 frequencies > 25%, with maxima of near 35% in the Fram Strait region (Fig. 3a). This is
 374 consistent with several previous studies which showed these regions have consistent influence (>
 375 15% of the time) from storms entering the Arctic (e.g., Clancy et al., 2022; Valkonen et al.,
 376 2021). This is also evident in the spatial distribution of MERRA-2 windspeeds (Fig. 3d), where
 377 the region of high blowing snow occurrence frequency is collocated with average windspeeds >
 378 6.5 m s⁻¹.
 379

380 The delineation between first- and multi-year sea ice (Tschudi et al., 2020) lies north of the Fram
 381 Strait and visibly bifurcates the region of elevated ICESat-2 derived blowing snow occurrence
 382 (Fig. 3a). In a recent study focused on Svalbard, Li et al. (2025) found that observed increases in

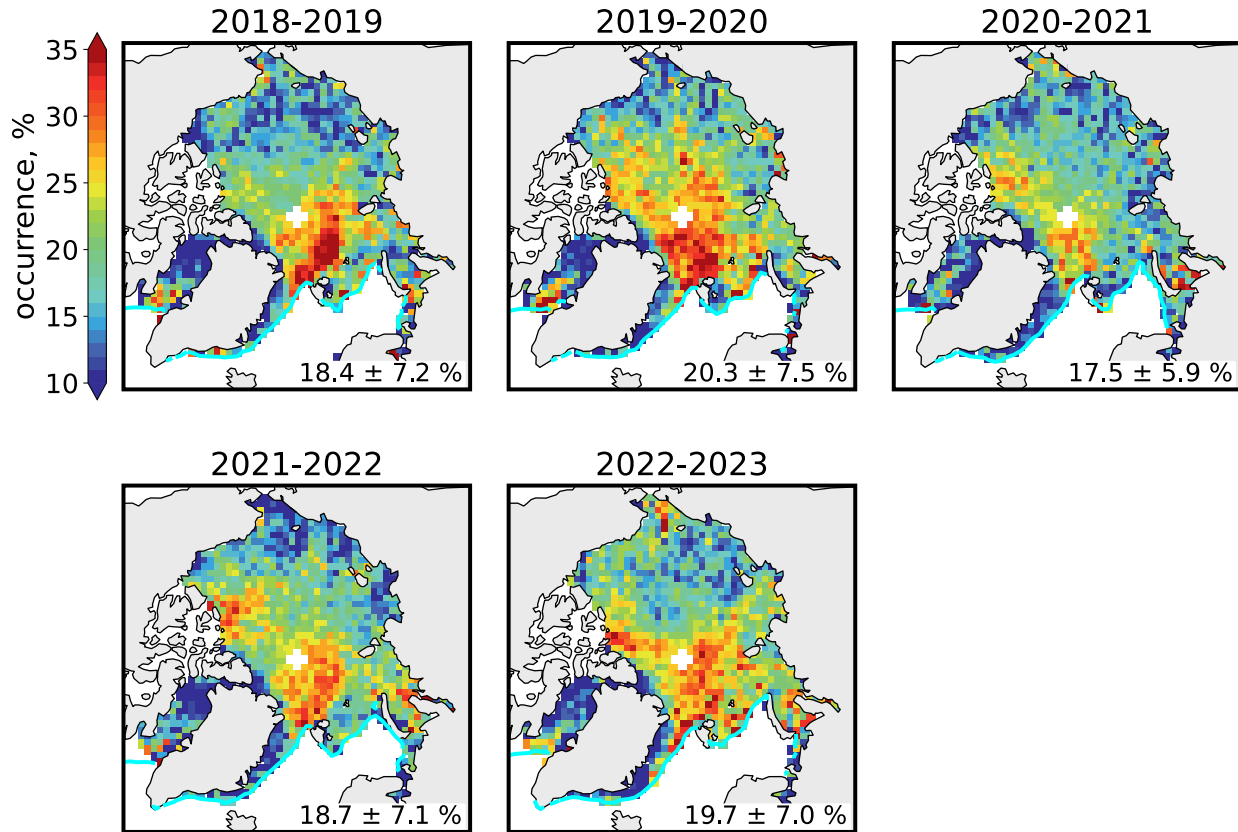
383 tropospheric bromine were correlated with air mass contact over sea ice under strong winds, and
 384 that boundary layer air masses reaching Svalbard spent more time over multi-year sea ice
 385 compared to first-year sea ice. The spatial pattern shown in Fig. 3a is consistent with these
 386 findings, where storms entering the Arctic drive strong north-northwesterly winds that
 387 preferentially advect air masses across the multi-year ice zone towards Svalbard.
 388



389 **Figure 3.** Mean ICESat-2 blowing snow properties during the cold season (November-April, 2018-2023): (a)
 390 occurrence frequency, (b) blowing snow geometrical depth, (c) optical depth, and (d) MERRA-2 10 m wind speed.
 391 The cyan line marks the 15% sea ice contour and the black line delineates regions of first- and multi-year sea ice
 392 (defined as multi-year ice constituting more than half of the total sea ice concentration). Numbers in the bottom right
 393 of each panel correspond to the mean and standard deviation for values over sea ice.
 394

395
 396 The ICESat-2 occurrence frequency does not include shallow (< 30 m thick) blowing snow
 397 layers, since these cannot be reliably detected at the vertical resolution of the atmospheric
 398 backscatter profiles. In addition, ICESat-2 cannot sample conditions where optically thick clouds
 399 prevent the surface from being detected. Regions of the Kara, Barents, and Greenland Seas are
 400 particularly susceptible to this under sampling, where the ICESat-2 cloud attenuated occurrence
 401 (% of all profiles where the surface cannot be detected) can exceed 50% across much of the cold
 402 season (Fig. S2).
 403

404 The multi-year cold season ICESat-2 retrievals show blowing snow layers averaging ~ 100 m in
 405 depth, ranging from ~ 50 m up to 160 m (Fig. 3b). Our previous analysis of ICESat-2
 406 observations near the 2019-2020 MOSAiC campaign demonstrated that low level turbulence
 407 often mixes blowing snow to the top of the surface inversion (Robinson et al., 2025), suggesting
 408 that blowing snow layer depth may serve as a useful indicator of Arctic inversion depth. Blowing
 409 snow optical depths average 0.12 across the Arctic, with maxima near 0.20 in the Fram Strait and
 410 southern Baffin Bay (Fig. 3c). These regions also experience thicker blowing snow layers on
 411 average. Figure 3 further shows that regions of deeper, optically thicker blowing snow are co-
 412 located with areas of high occurrence frequency and stronger winds.
 413



414
415
416
417
418
419

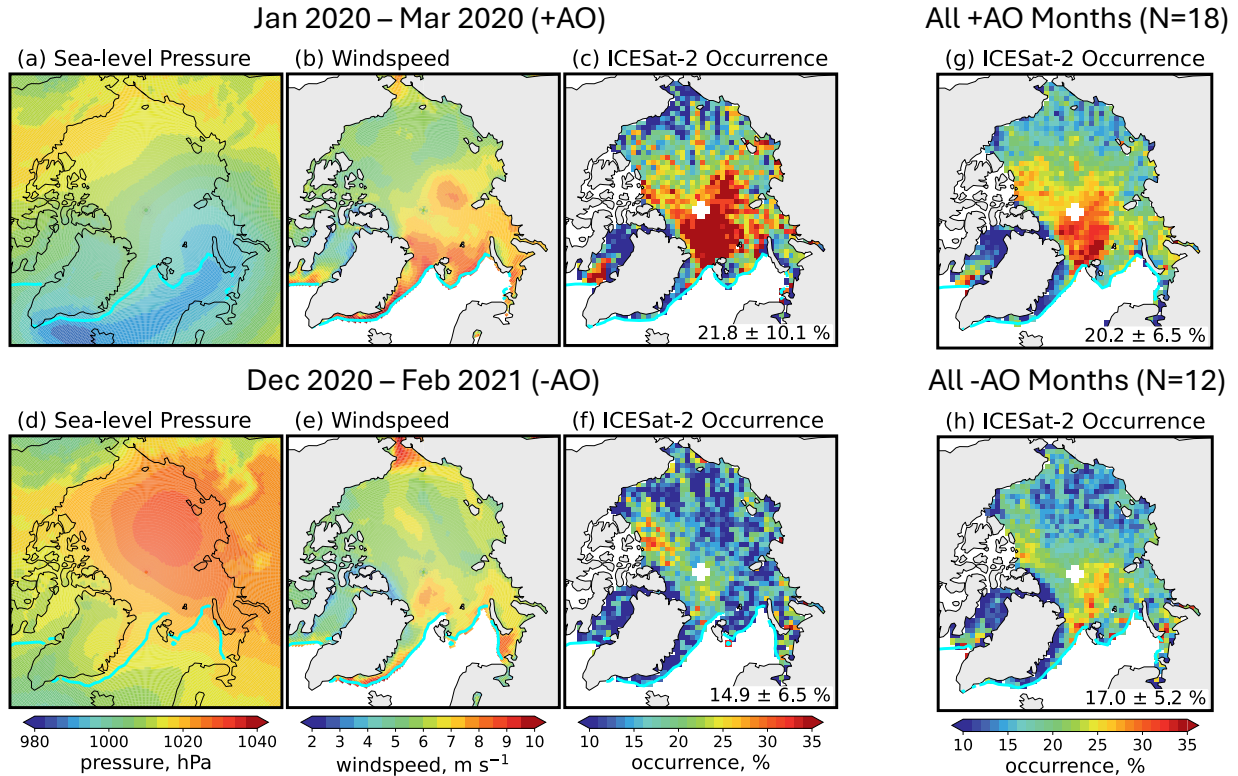
Figure 4. Interannual spatial variability of blowing snow occurrence frequency (units %) from ICESat-2 observations during the 2018-2023 cold seasons. Each panel shows the average pan-Arctic occurrence and standard deviation (lower right). The cyan line marks the 15% sea ice concentration contour.

420 Figure 4 shows that the ICESat-2 pan-Arctic blowing snow occurrence frequencies are consistent
421 from year-to-year at 18-20%. The spatial pattern of occurrence also remains fairly consistent,
422 with the Central Arctic and Fram Strait displaying the highest frequencies and only moderate
423 shifts in location. Despite this, the Central Arctic can display substantial year-to-year variability.
424 For example, the highest (2019-2020) and lowest (2020-2021) pan-Arctic frequencies were
425 observed in consecutive cold seasons.

426

427 The contrast between these two cold seasons appears closely aligned with large scale climate and
428 atmospheric circulation patterns, particularly the Beaufort High and the Arctic Oscillation (AO).
429 In early 2020, a record positive AO phase (+3.5, top row Fig. S3) coincided with a collapse of
430 the Beaufort High, enhanced cyclone activity (Ballinger et al., 2021; Rinke et al., 2021), and
431 widespread blowing snow. From January to March 2020, MERRA-2 sea-level pressure (SLP)
432 and windspeed featured an elongated region of consistently low pressure (< 1,000 hPa) extending
433 from Iceland into the ice-covered Kara and Barents Seas (Fig. 5a). Over these regions and the
434 Central Arctic, mean windspeeds reached 7-9 m s⁻¹ (Fig. 5b). During this period, ICESat-2
435 observed several intense blowing snow episodes covering more than 25% of sea ice area
436 (blowing snow > 1×10⁶ km²; Fig. S4), with mean pan-Arctic blowing snow frequencies of
437 21.8%, reaching up to 50% in the Central Arctic (Fig. 5c).

438



439
440
441
442
443
444
445

Figure 5. Comparison of (a,d) MERRA-2 sea-level pressure (hPa), (b,e) MERRA-2 wind speed (m s^{-1}), and (c,f) ICESat-2 observed blowing snow occurrence frequency (%) for January 2020 – March 2020 (a-c) and December 2020 – February 2021 (d-f). (g,h) Composite ICESat-2 blowing snow occurrence frequency for months with (g) positive and (h) negative Arctic Oscillation phases during the 2018-2023 cold seasons.

446
447
448
449
450
451
452
453
454
455
456
457

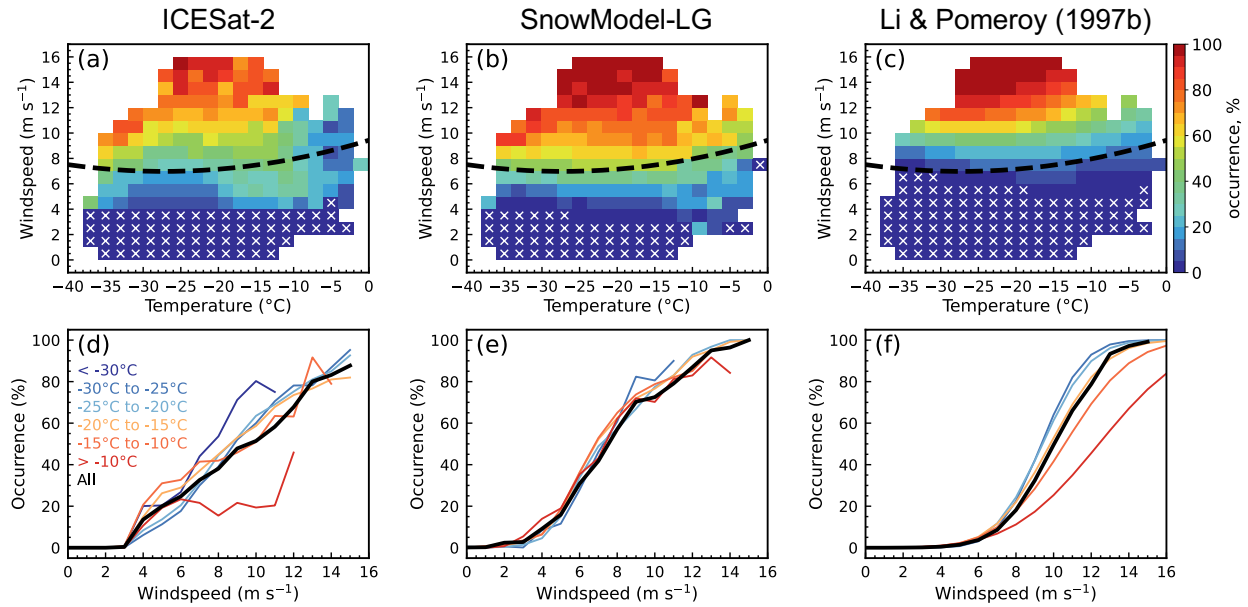
In contrast, the 2020-2021 season was marked by a strong negative AO (-2.4, top row Fig. S3) and a persistent Beaufort High (mean MERRA-2 SLP > 1,020 hPa across most of the Arctic basin, Fig. 5d), conditions known to suppress storm activity (Kenigson & Timmermans, 2021; Serreze & Barrett, 2011). Consistent with this pattern, MERRA-2 windspeeds were on average $\sim 2 \text{ m s}^{-1}$ lower relative to January-March 2020 (Fig. 5e). From December 2020 to February 2021 ICESat-2 detected substantially less blowing snow (47% lower relative to Jan-Mar 2020), with frequencies in the Central Arctic maximizing at only $\sim 25\%$ (Fig. 5f). Across all months, we find a moderately strong correlation between AO phase and ICESat-2 blowing snow occurrence ($r = 0.62$; Fig. S3c). Composites highlight this relationship: positive AO months (N=18; Fig. 5g) exhibit 20% more blowing snow than negative AO months (N=12, Fig. 5h), with particularly large differences (up to a factor of two) in the Fram Strait and Central Arctic.

458
459

3.2 Relationship between windspeed and blowing snow

460
461
462
463
464
465

In the following section we focus on the Central Arctic region during January-March, the region most well-sampled by ICESat-2 and months least affected by optically thick clouds (Fig. S2). To examine relationships between meteorological factors and blowing snow, we use daily 100 km grid-cell averages. Although this lowers the total number of samples compared to a profile-based approach, averaging helps to reduce noise.



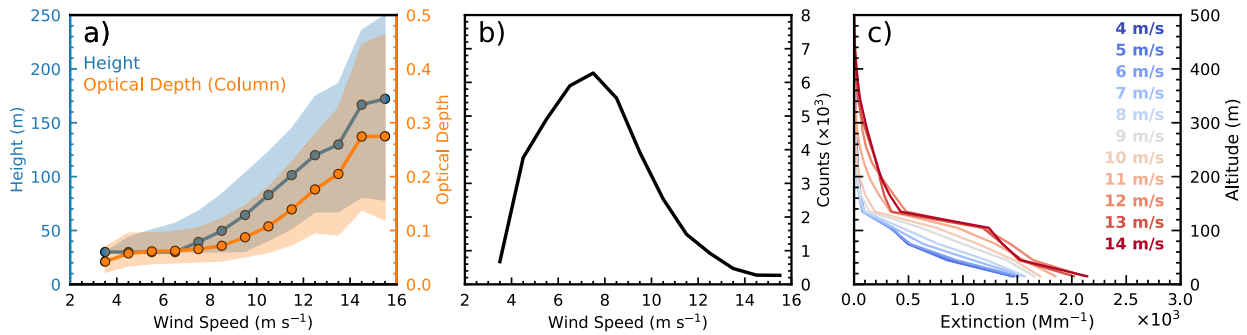
466
467
468 **Figure 6.** Top row: Dependence of blowing snow occurrence frequency on windspeed and temperature for (a)
469 ICESat-2, (b) SnowModel-LG (blowing snow transport fluxes > 0.20 Mg m⁻¹ d⁻¹), and (c) Li & Pomeroy (1997b)
470 (mean snow age = 72 hours). White stippling represents conditions with no blowing snow; the black dashed line
471 shows the DY2001 threshold windspeed. Bottom row: Dependence of blowing snow occurrence frequency on
472 windspeed for all temperatures (black), and for different temperature ranges (< -30°C; -30° to -25°C; -25° to -20°C;
473 -20° to -15°C; -15° to -10°C; > -10°C) for (d) ICESat-2, (e) SnowModel-LG, and (f) Li & Pomeroy (1997b).
474

475 Figure 6 compares the blowing snow occurrence as a function of windspeed and temperature.
476 For comparison to ICESat-2 and SnowModel-LG, the blowing snow occurrence from Li &
477 Pomeroy (1997b) is also shown (see their Eq. 7). The blowing snow occurrence from Li &
478 Pomeroy (1997b) is based on a statistical analysis of observations for 16 stations on the prairies
479 of western Canada and is a function of windspeed, temperature, and snow age (assumed in our
480 analysis to be 72 hours). It is also in contrast to DY2001, where the threshold windspeed
481 essentially acts as an on-off switch for blowing snow. ICESat-2 retrievals indicate a 10-40%
482 blowing snow occurrence below the DY2001 threshold of ~ 7 m s⁻¹ (black dashed line, Fig. 6a),
483 with a much stronger dependence on windspeed than on temperature (Fig. 6a). For example, at 8
484 m s⁻¹, the ICESat-2 occurrence is 50-60% across all temperatures, while at -25 °C it rises from
485 10-15% at 4 m s⁻¹ to > 80% at 15 m s⁻¹. SnowModel-LG predictions (defined as blowing snow
486 transport > 0.20 Mg m⁻¹ d⁻¹) display frequencies ~10% larger than ICESat-2 on average but
487 capture similar features (Fig. 6b). The occurrence of blowing snow predicted from Li & Pomeroy
488 (1997b) displays a narrower transition region, increasing sharply from < 20% to > 60% over the
489 8-10 m s⁻¹ range (Fig. 6c).

490
491 The one-dimensional distributions (Fig. 6d-f) further emphasize the dominant control of
492 windspeed, with all three datasets showing increasing occurrence with stronger winds. ICESat-2
493 and SnowModel-LG show a weak temperature dependence, with slightly lower occurrence at
494 higher temperatures, especially for stronger winds, consistent with enhanced snow cohesion and
495 bonding resistance (Fig. 6d,e). The Li & Pomeroy (1997b) formulation shows a stronger
496 temperature sensitivity, ranging from 75% at T < -30 °C to 20% at T > -5 °C for a 10 m s⁻¹
497 windspeed (Fig. 6e). The temperature dependence is likely stronger because of our assumption of

498 a fixed snow age of 72 hours. Snow age also influences bonding and cohesion, with older snow
 499 being more resistant to erosion. Because SnowModel-LG and ICESat-2 sample a range of snow
 500 ages, their apparent temperature dependence is likely weaker.

501
 502 ICESat-2 blowing snow properties also show a strong dependence on windspeed (Fig. 7a).
 503 Median blowing snow layer height increases from 30 m at windspeeds of $\sim 4 \text{ m s}^{-1}$ to more than
 504 150 m at windspeeds $> 14 \text{ m s}^{-1}$. Optical depth exhibits a similar relationship, rising from 0.02
 505 0.26 over the same windspeed range. The spread in both height and optical depth (shading, Fig.
 506 7a) also widens with increasing windspeed, which we attribute to increased noise from fewer
 507 observations in the highest windspeed bins (Fig. 7b).
 508



509
 510
 511 **Figure 7.** Dependence of ICESat-2 blowing snow height and optical depth on windspeed. **(a)** Median (circles with
 512 line) and interquartile range (shading) of ICESat-2 retrieved blowing snow geometric depth (blue) and optical depth
 513 (orange) as a function of 10 m windspeed, using 0.5 m s^{-1} bins. **(b)** Number of grid cells (in thousands) in each
 514 windspeed bin from panel a. **(c)** Mean blowing snow extinction profiles (units Mm^{-1}) from ICESat-2 retrievals in
 515 February 2022 ($N = 678,914$), grouped in 1 m s^{-1} wide windspeed bins.

516
 517 The increase in blowing snow optical depth reflects a combination of increased blowing snow
 518 height and stronger backscatter signal (Fig. 7c). Across nearly 700,000 ICESat-2 retrievals in
 519 February 2022, near-surface blowing snow extinction increased by 40% from $1.5 \times 10^3 \text{ Mm}^{-1}$ at 4
 520 m s^{-1} to $2.1 \times 10^3 \text{ Mm}^{-1}$ at 14 m s^{-1} . The enhancement is even larger aloft (a factor of 2-3).
 521 Together, these results indicate that stronger winds loft more blowing snow higher into the
 522 atmosphere, consistent with previous studies (Palm et al., 2011, 2018; Robinson et al., 2025).
 523

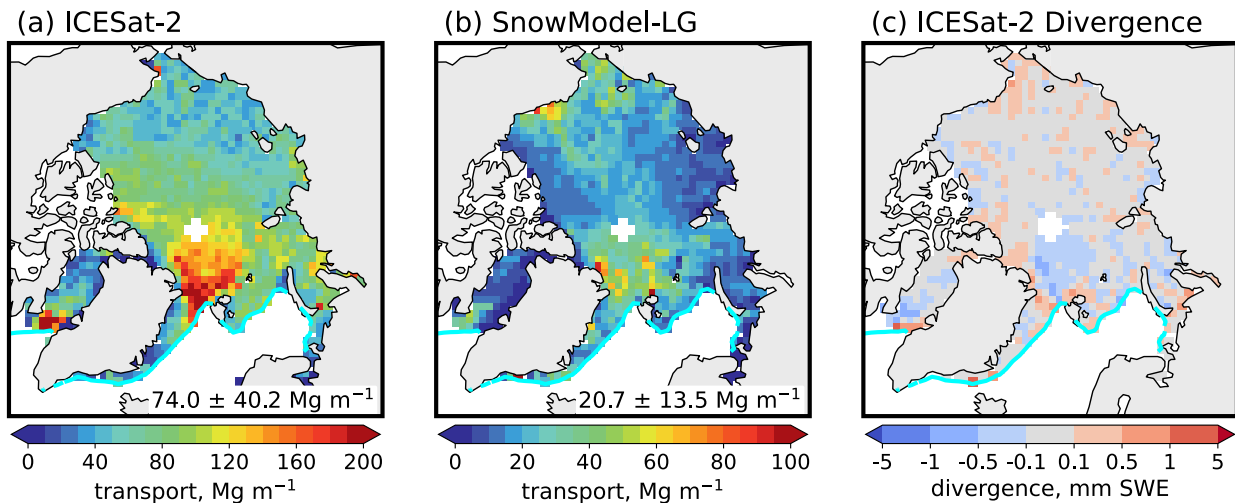
524 4 Contribution of blowing snow to the Arctic snow-on-sea ice budget

525
 526 In this section we examine the contribution of blowing snow to the Arctic cold season snow-on-
 527 sea-ice budget. We focus on column integrated blowing snow mass transport (Q_t in Eq. 1) and
 528 sublimation (Q_{bs} in Eq. 1) fluxes, placing them in the context of one another and comparing them
 529 to accumulated snowfall. When interpreting the magnitude of the ICESat-2 estimates, we note
 530 that they depend on assumptions inherent to the backscatter-to-flux conversions (Palm et al.,
 531 2017; Robinson et al., 2025), including prescribed blowing snow particle sizes and the use of
 532 modeled meteorological fields to represent near-surface windspeed, temperature, and humidity
 533 (section 2.1). Blowing snow particle sizes are assumed to decrease exponentially with height,
 534 while sublimation rates increase with higher temperatures and lower humidities.
 535
 536

537 **4.1 Blowing snow transport from ICESat-2 and SnowModel-LG**

538

539 Figure 8 shows the spatial distribution of blowing snow transport flux inferred from ICESat-2.
540 The flux is calculated by combining the ICESat-2 derived mass concentrations with the vertical
541 profile of windspeed, integrated over the depth of the blowing snow layer. The pan-Arctic mean
542 transport flux observed by ICESat-2 is 74 Mg m^{-1} , with maxima $> 160 \text{ Mg m}^{-1}$ in the Central
543 Arctic, co-located with regions of frequent and intense blowing snow (Fig. 3). SnowModel-LG
544 produces a similar spatial distribution but yields transport fluxes that are 2-3 times lower. This
545 discrepancy likely arises because SnowModel-LG confines blowing snow to the lowest several
546 meters of the atmosphere, where winds are weaker. In contrast, ICESat-2 detects blowing snow
547 layers extending several hundred meters above the surface (Fig. 3b, 7a), where stronger winds
548 enhance snow transport. To support this interpretation, we examined the pan-Arctic blowing
549 snow burdens (mass per square meter; Fig. S5) and found that they agree to within about 20%
550 between ICESat-2 (0.17 g m^{-2}) and SnowModel-LG (0.14 g m^{-2}). In the Central Arctic regions of
551 enhanced transport, both datasets have mean blowing snow burdens of up to 0.40 g m^{-2} .
552



553

554

555 **Figure 8.** Mean 2018-2023 cold season blowing snow transport flux (Mg m^{-1}) from (a) ICESat-2 and (b)
556 SnowModel-LG. Note the color scale for SnowModel-LG is different than for ICESat-2. (c) Divergence of blowing
557 snow transport inferred from ICESat-2 (mm SWE).
558

559 Although the spatial pattern of transport broadly agrees, our seasonal values are smaller than
560 those reported by J. Yang et al. (2010). Their simulations for December 2006 – February 2007
561 suggested transport fluxes up to 800 Mg m^{-1} in the Central Arctic and $> 1,000 \text{ Mg m}^{-1}$ along
562 Greenland's east coast. These higher values could reflect methodological differences: their
563 model did not explicitly account for variable snowpack conditions, which could lead to an
564 overestimate in blowing snow occurrence and transport, and was run at finer spatial (18 km) and
565 temporal (5 s) resolutions, which could capture small-scale wind gradients and localized
566 enhancements in snow redistribution. Despite these differences, both our results and those of J.
567 Yang et al. (2010) indicate that blowing snow transport plays a relatively minor role in the basin-
568 scale snow budget. For example, the divergence of ICESat-2 transport (Fig. 8c) is limited to a
569 few tenths of mm SWE, with localized maxima near 1 mm SWE in regions of frequent blowing
570 snow. We further examined the divergence separately for each cold season (Fig. S6), finding that

571 basin-wide averages remain $< 10^{-3}$ mm SWE. The divergence exhibits interannual variability
572 which is largely tied to prevailing meteorological conditions and blowing snow occurrence. For
573 example, we find substantially greater ICESat-2 inferred divergence during 2019-2020 compared
574 to 2020-2021, consistent with the AO-phase dependence of blowing snow discussed above (Fig.
575 5).

576

577 **4.2 Multi-year estimates of blowing snow sublimation**

578

579 Figure 9 shows the mean total annual blowing snow sublimation and snowfall for the 2018-2023
580 cold seasons. Pan-Arctic blowing snow sublimation totals from ICESat-2 (1.63 cm SWE) are in
581 close agreement with SnowModel-LG (1.66 cm SWE) and within 30% of DY2001 (2.07 cm
582 SWE). All three estimates are broadly consistent with previous modeling studies (Chung et al.,
583 2011; Liston et al., 2020; J. Yang et al., 2010). In the Central Arctic near Svalbard, ICESat-2
584 indicates the highest values of sublimation (3-4 cm SWE). A secondary maximum (> 3 cm SWE)
585 occurs in the Barents Sea, where blowing snow is retrieved half as often. This reflects the
586 sensitivity of sublimation to temperature and humidity, because the marginal seas are generally
587 warmer than the Central Arctic (Fig. S7). Thus, the reduced occurrence of blowing snow is offset
588 by higher temperatures and lower humidity, which enhance sublimation.

589

590 The average blowing snow sublimation derived from ICESat-2 over first-year sea ice is 1.47 cm
591 SWE (SnowModel-LG: 1.66 cm SWE; DY2001: 2.02 cm SWE), compared to 2.06 cm SWE
592 over multi-year ice (SnowModel-LG: 1.81 cm SWE; DY2001: 2.21 cm SWE). While multi-year
593 ice constitutes only 25% of our study area, it accounts for 30-35% of the seasonal blowing snow
594 sublimation. This disproportionate contribution is consistent with the spatial pattern of blowing
595 snow shown above (Fig. 3), where the region of elevated winds and occurrence is split by the
596 transition between first- and multi-year ice.

597

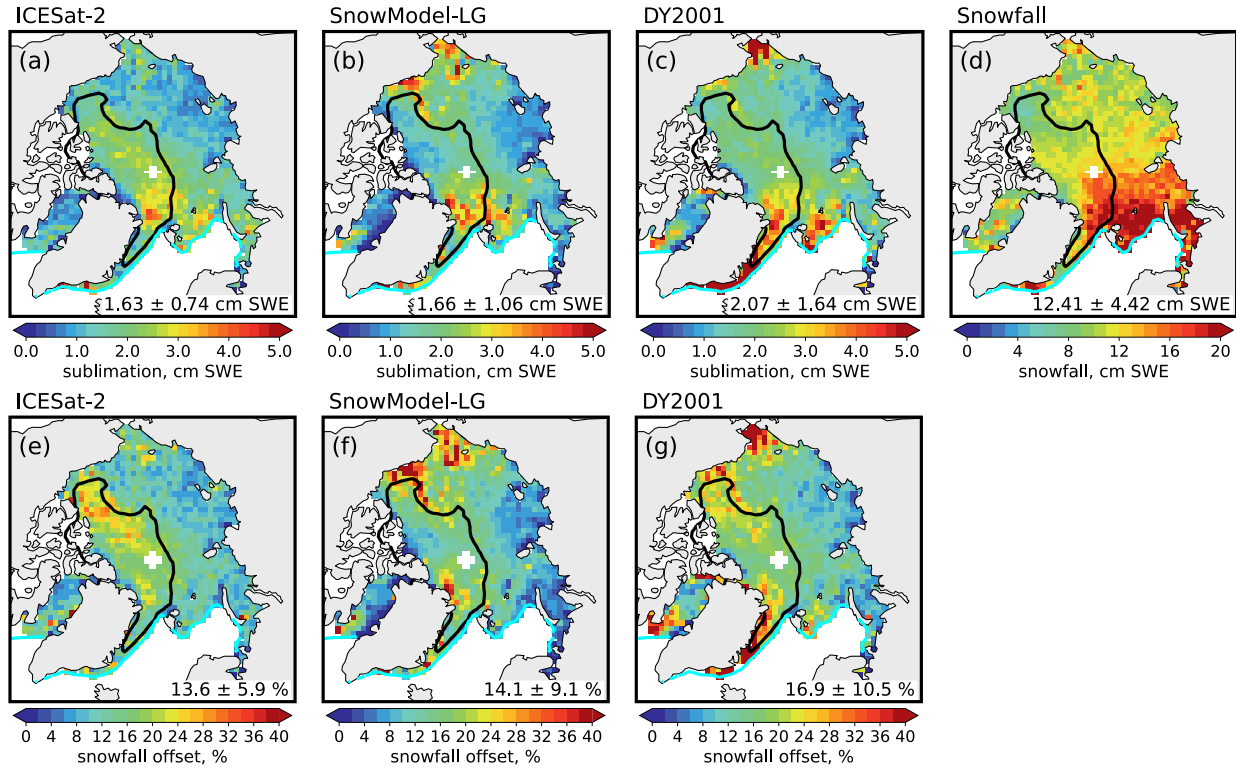
598 We compare blowing snow sublimation to total MERRA-2 snowfall over the cold season (12.41
599 cm SWE, Fig. 9d). On average, we find that blowing snow removes 13.6% (ICESat-2), 14.1%
600 (SnowModel-LG), and 16.9% (DY2001) of snowfall. The regional impact, however, varies
601 strongly (Figs. 9e-g). In the Kara and Barents Seas, where snowfall is highest, sublimation
602 removes only 5-10% of snowfall. In the Central Arctic losses increase to 18-24%, while in
603 regions with more moderate snowfall, such as the Beaufort Sea, sublimation losses can exceed
604 30% (e.g., 2-3 cm SWE of sublimation compared to 8-10 cm SWE of snowfall).

605

606 The fraction of snowfall removed by blowing snow sublimation inferred from ICESat-2 reaches
607 30% in the Beaufort Sea north of the Canadian Arctic Archipelago (Fig. 9e). SnowModel-LG
608 and DY2001 show a similar enhanced offset, though their maxima are shifted southeastward
609 along the coast of Alaska (Fig. 9f,g). The 2018-2023 period was marked by several strong
610 Beaufort High episodes, such as the 2020-2021 event highlighted in Fig. 5, which are typically
611 associated with calm, dry conditions. Under such conditions, ICESat-2 retrievals may
612 occasionally overestimate blowing snow. False positives could arise when low-level ice crystals
613 (ice clouds or diamond dust) mix with blowing snow, leading the entire ICESat-2 backscatter
614 signal to misattributed to blowing snow. This effect was most pronounced during winter 2021-
615 2022, when exceptionally warm ($T > -20^{\circ}\text{C}$) and dry ($\text{RH}_{\text{ice}} < 90\%$) conditions prevailed north of
616 the Canadian Arctic Archipelago (Fig. S8).

617
618
619
620
621
622

The fraction of snowfall removed by blowing snow sublimation, as inferred from ICESat-2, also varies by ice type. On average, values over multi-year ice (15-22%) are 1.6 times larger than over first-year ice (9-14%). The enhanced offsets reflects both stronger sublimation and overall lower snowfall over multi-year ice (11.43 cm SWE) compared to first-year ice (12.64 cm SWE).



623
624
625
626
627
628
629
630

Figure 9. Spatial distribution of blowing snow sublimation, total snowfall, and the contribution of blowing snow sublimation to snowfall offset over Arctic sea ice during 2018-2023. **(a-c)** Total blowing snow sublimation (cm SWE) inferred from (a) ICESat-2, (b) SnowModel-LG, and (c) DY2001. **(d)** Total MERRA-2 snowfall (cm SWE). **(e-g)** Percent of snowfall removed by blowing snow sublimation ($= 100 \times [\text{sublimation} / \text{snowfall}]$) from (e) ICESat-2, (f) SnowModel-LG, and (g) DY2001. The cyan line marks the 15% sea ice concentration contour and the black line delineates regions of first- and multi-year sea ice.

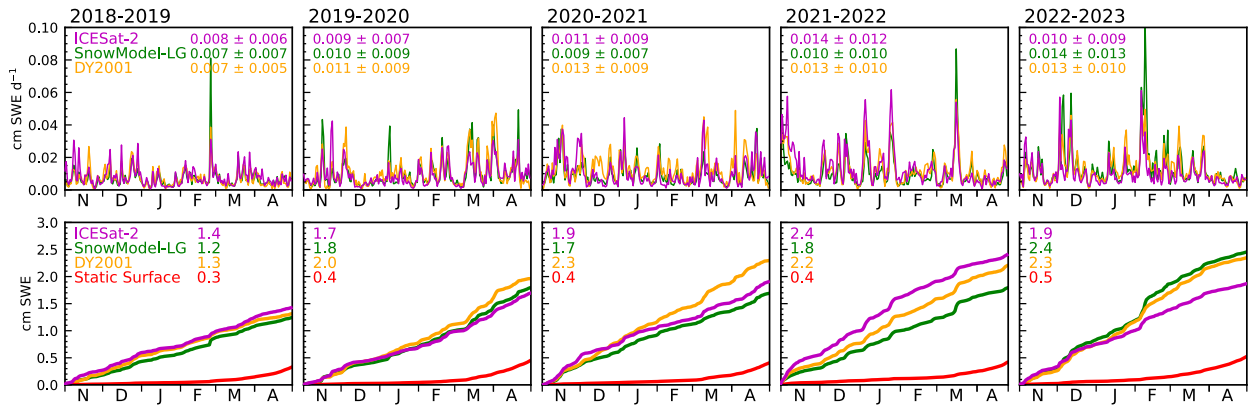
631
632
633
634
635
636
637

Along Greenland's east coast, DY2001 predicts much higher sublimation fluxes (4-5 cm SWE, > 70% of snowfall) than either ICESat-2 and SnowModel-LG (2-3 cm SWE, 20-30% of snowfall). This discrepancy likely reflects DY2001's simple threshold-based parameterization, which tends to overpredict blowing snow at the typical windspeeds in this region (6-8 m s⁻¹, Fig. 3). Warmer and drier conditions in this region (Fig. S7) further amplify the sublimation predicted by DY2001.

638
639
640
641
642
643

Daily pan-Arctic time series (Fig. 10) show that blowing snow sublimation is nearly continuous throughout the cold season, punctuated by sharp peaks during major storm events. The most intense episodes (> 0.04 cm SWE d⁻¹ averaged over sea ice) occur only a few times per season and correspond to widespread blowing snow detected by ICESat-2 (Fig. S4). These storms contribute disproportionately to the seasonal total, with individual events removing up to 60% of daily snowfall (Fig. S9). Between storms, sublimation persists at lower but steady rates (0.01-

644 0.02 cm SWE d⁻¹) and these background losses accumulate to a substantial share (35-40%) of the
 645 seasonal total.
 646



647
 648
 649 **Figure 10.** Timeseries of blowing snow sublimation across five Arctic cold seasons. **(top row)** Daily blowing snow
 650 sublimation (cm SWE d⁻¹) inferred from ICESat-2 (magenta line) and predicted by SnowModel-LG (green line) and
 651 DY2001 (orange line). **(bottom row)** Cumulative daily blowing snow sublimation (cm SWE). The red lines in the
 652 bottom row represent the cumulative static surface (non-blowing snow) sublimation predicted by SnowModel-LG.
 653

654 The ICESat-2 inferred sublimation ranges from 1.4 to 2.4 cm SWE across the five cold seasons
 655 (Fig. 10, bottom row), corresponding to a 11-20% offset of seasonal snowfall. Both snowfall and
 656 blowing snow sublimation vary by 1-2 cm SWE year to year, but the two do not always covary.
 657 For example, the 2021-2022 cold season had the lowest snowfall (11.9 cm SWE) yet the highest
 658 ICESat-2 sublimation (2.4 cm SWE, 20% offset). Conversely, 2018-2019 featured higher
 659 snowfall (12.9 cm SWE) but relatively low sublimation (1.4 cm SWE, 11% offset). These
 660 interannual differences highlight that sublimation depends not only on storm frequency and
 661 strength (which also drive snowfall) but also on atmospheric conditions which regulate blowing
 662 snow occurrence and sublimation efficiency. SnowModel-LG and DY2001 generally agree with
 663 the ICESat-2 sublimation, though DY2001 tends to predict slightly higher values.
 664

665 Blowing snow sublimation exceeds surface sublimation by a factor of 4-5, underscoring the
 666 dominant role of blowing snow in sublimation-driven snow loss during much of the cold season.
 667 The cumulative surface sublimation timeseries (Q_{ss} in Eq. 1) predicted by SnowModel-LG is
 668 shown in Fig. 10 (red lines, bottom row). Seasonal total surface sublimation averages only 0.3-
 669 0.5 cm SWE, with nearly all of it occurring from late February through April, when solar
 670 radiation increases, near-surface air warms, and RH_{ice} decreases. These values are lower than the
 671 1-2 cm SWE reported by Déry and Yau (2002), likely because their annual means included the
 672 warmer spring and summer months. Consistent with this, SnowModel-LG calculates an Arctic-
 673 wide annual mean surface sublimation of ~ 1 cm SWE.
 674

675 ICESat-2 likely underestimates blowing snow sublimation because it cannot observe blowing
 676 snow beneath optically thick clouds. These conditions are most frequent during winter storms,
 677 when strong winds can drive intense sublimation. To assess this sampling bias, we examine the
 678 2018-2023 SnowModel-LG and DY2001 predictions under all conditions (i.e., regardless of
 679 whether ICESat-2 detected the surface). The all-conditions maps (Fig. S10) show patterns similar
 680 to Fig. 9 but with magnitudes 16-25% larger. Pan-Arctic blowing snow sublimation totals

681 increase to 2.1 cm SWE for SnowModel-LG and 2.4 cm SWE for DY2001. Comparing these
682 values to the seasonal snowfall from Fig. 9 (12.4 cm SWE) yields offsets of 17% for
683 SnowModel-LG and 19% for DY2001. This comparison suggests that ICESat-2 captures the
684 spatial pattern and temporal variability of blowing snow sublimation well but underestimates the
685 total by roughly 20% due to this sampling bias.

686

687 **5 Summary and conclusions**

688

689 We presented the first multi-year pan-Arctic estimates of blowing snow derived from ICESat-2
690 satellite observations, extending our earlier single-year analysis (Robinson et al., 2025) to five
691 cold seasons (November through April, 2018-2023). ICESat-2 retrievals allowed us to
692 characterize blowing snow occurrence and properties (geometric and optical depths), and, when
693 combined with assumptions about particle sizes and meteorology from reanalysis, to infer
694 blowing snow sublimation and evaluate its contribution to the Arctic snow-on-sea ice budget.

695

696 Over the five seasons analyzed, ICESat-2 retrievals indicate a mean pan-Arctic blowing snow
697 occurrence of 19%, with maxima exceeding 30% in the Central Arctic and Atlantic sector,
698 regions frequently impacted by storms arriving from lower latitudes. Retrieved blowing snow
699 geometric and optical depths also maximize in these regions. Interannual variability of blowing
700 snow occurrence is substantial and is driven by the Arctic Oscillation (AO). We find that positive
701 AO periods have lower SLP and higher winds, and $\sim 50\%$ more blowing snow than negative AO
702 periods. In the Central Arctic, blowing snow occurrence during the positive AO phase was more
703 than twice that of the negative phase, a pattern consistent across all five seasons.

704

705 ICESat-2 observations confirm that windspeed is the primary driver of blowing snow
706 occurrence, with temperature acting as a secondary modulating factor. Blowing snow occurrence
707 increases with windspeed across all temperatures, exceeding 80% at 12 m s^{-1} . The physics-based
708 threshold windspeed in SnowModel-LG ($4\text{-}5 \text{ m s}^{-1}$) is $2\text{-}3 \text{ m s}^{-1}$ lower than in DY2001 ($\sim 7 \text{ m s}^{-1}$)
709 and aligns more closely with the windspeeds at which ICESat-2 reliably detects blowing snow.
710 Both ICESat-2 and SnowModel-LG suggest blowing snow occurrence frequencies of 10-40% at
711 windspeeds $4\text{-}7 \text{ m s}^{-1}$, where DY2001 predicts no blowing snow. Windspeed also strongly
712 controls blowing snow height and optical depth: blowing snow heights increase from 30 m at 4
713 m s^{-1} to almost 200 m at 15 m s^{-1} , while optical depths rise from 0.02 to 0.26 over the same
714 range, driven by enhanced backscatter over deeper heights.

715

716 Maximum mass transport fluxes peak where blowing snow is most frequent, with seasonal means
717 of 74 Mg m^{-1} for ICESat-2 and 21 Mg m^{-1} for SnowModel-LG. This factor of three difference
718 reflects SnowModel-LG's confinement of blowing snow to the lowest few meters, where winds
719 are weaker, while ICESat-2 detects layers extending to several hundreds of meters, where
720 stronger winds drive greater transport. Yet, pan-Arctic burdens agree within $\sim 20\%$ (0.17 g m^{-2}
721 for ICESat-2 vs. 0.14 g m^{-2} for SnowModel-LG), underscoring that while the vertical extent is
722 different, the overall mass is consistent. Despite high transport, divergence in ICESat-2 inferred
723 mass flux contributes minimally to the snow budget (maximum of 1 mm SWE).

724

725 We find that blowing snow sublimation plays an important role in the Arctic snow-on-sea-ice
726 budget, reaching up to 5 cm SWE in the Central Arctic, and averaging 1.63-2.07 cm SWE over

727 all sea ice. This is equivalent to a 13.6-16.9% removal of seasonal snowfall on average, with as
728 much as 30% removal in some regions such as the Beaufort Sea. Blowing snow sublimation
729 derived from ICESat-2 is consistently larger over multi-year sea ice (2.06 cm SWE) than first-
730 year sea ice (1.47 cm SWE), corresponding to a 1.6 times larger fraction of snowfall removed
731 (15-22% vs. 9-14%). The pan-Arctic ICESat-2 inferred blowing snow sublimation ranged from
732 1.4 to 2.4 cm SWE (11-20% snowfall offset) across the five cold seasons, with similar estimates
733 from SnowModel-LG (1.2-2.4 cm SWE) and DY2001 (1.3-2.3 cm SWE). SnowModel-LG and
734 DY2001 predictions under all conditions (i.e., including those without ICESat-2 observations
735 due to sampling or clouds) suggest pan-Arctic blowing snow sublimation could be ~20% larger
736 (2.1-2.4 cm SWE) than was found using ICESat-2, resulting in a larger snowfall removal of 17-
737 19%. SnowModel-LG indicates that sublimation from blowing snow is up to a factor of five
738 larger than surface sublimation, which offsets only an additional 2-4% of snowfall.

739
740 Our analysis is limited by a number of factors, including the sampling pattern of ICESat-2.
741 While the high resolution of atmospheric backscatter allows unprecedented detail into blowing
742 snow, the narrow spatial sampling requires temporal and spatial averaging, such as binning the
743 ICESat-2 profiles to a 100 km grid, to generate meaningful statistics. This approach improves
744 coverage but smooths fine-scale variability and may underrepresent short-lived or localized
745 blowing snow events. Moreover, the blowing snow algorithm cannot detect blowing snow layers
746 thinner than 20-30 m. Such thin drifting and blowing snow layers are often predicted by
747 SnowModel-LG and DY2001. Nevertheless, these discrepancies in vertical resolution and
748 sampling appear to have a minimal net effect on the overall estimates of blowing snow fluxes,
749 which are similar for all three methods. Our transport and sublimation flux estimates rely on
750 reanalysis meteorology, which has been shown to have biases, particularly at high latitudes (e.g.,
751 Jonassen et al., 2019; Marshall et al., 2018), and currently does not include feedbacks from
752 blowing snow on the temperature and moisture fields. Such feedbacks would tend to suppress
753 sublimation by increasing humidity and cooling the near-surface atmosphere, potentially leading
754 to overestimation of sublimation in our analysis. However, work done on Antarctic blowing
755 snow processes indicates that the entrainment of warmer and drier air present above the blowing
756 snow and surface temperature inversion can reduce or even eliminate this sublimation-humidity
757 feedback (Palm et al., 2018). Incorporating these processes into coupled models would improve
758 the realism of both meteorological forcing and snow-atmosphere interactions.

759
760 Beyond its role in the snow-on-sea-ice budget, blowing snow sublimation also acts as a
761 significant source of moisture and a sink of heat for the atmosphere. The fate of this moisture
762 remains poorly constrained and warrants further study. Blowing snow sublimation over sea ice is
763 also a recognized source of sea salt aerosols (e.g., Frey et al., 2020; Gong et al., 2023; Huang &
764 Jaeglé, 2017; Ranjithkumar et al., 2025). Taken together, these points highlight that blowing
765 snow has the potential to impact a range of polar processes including boundary layer structure,
766 cloud formation and lifetime, atmospheric chemistry, and the surface energy balance. Recent
767 modeling efforts are beginning to account for these processes (e.g., Hofer et al., 2021; Luo et al.,
768 2021), offering new opportunities to improve predictions of Arctic composition, weather, and
769 climate. Such advancements will require robust observational constraints to ensure realism and
770 guide a process-based understanding of the coupled Arctic system. By capturing the vertical and
771 horizontal structure of blowing snow at unprecedented scales, our study demonstrates that

772 spaceborne lidar is a key tool for bridging the gap between observations and models, and for
773 advancing our understanding of the rapidly changing Arctic environment.

774
775
776
777
778

779 **Code and data availability**

780
781
782
783

The ICESat-2 ATLAS data used in this study can be accessed through the NASA NSIDC Distributed Active Archive Center (<https://doi.org/10.5067/ATLAS/ATL09.006>). The code and data required to reproduce the figures in this study are available at: <https://doi.org/10.5281/zenodo.18119606>.

784
785

786 **Author contributions**

787
788
789

JR and LJ designed the study. SPP aided in ICESat-2 software development and visualization. GEL developed the SnowModel-LG code. JR and LJ performed formal analysis. JR prepared the manuscript with contributions from all co-authors.

790
791

792 **Competing interests**

793
794

The authors declare that they have no conflict of interest.

795
796

797 **Acknowledgments**

798
799

The authors express gratitude to the ICESat-2 engineering and science teams for their ongoing efforts to maintain the ATLAS instrument and generate the ICESat-2 atmospheric data products.

800
801

802 **References**

803
804
805
806
807
808
809
810
811
812
813
814
815
816
817
818
819
820
821

- Ballinger, T. J., Walsh, J. E., Bhatt, U. S., Bieniek, P. A., Tschudi, M. A., Brettschneider, B., Eicken, H., Mahoney, A. R., Richter-Menge, J., & Shapiro, L. H.: Unusual West Arctic Storm Activity During Winter 2020: Another Collapse of the Beaufort High? *Geophysical Research Letters*, 48(13). <https://doi.org/10.1029/2021gl092518>, 2021.
- Bintanja, R.: The impact of Arctic warming on increased rainfall. *Scientific Reports*, 8(1), 16001. <https://doi.org/10.1038/s41598-018-34450-3>, 2018.
- Bintanja, R., & Andry, O.: Towards a rain-dominated Arctic. *Nature Climate Change*, 7(4), 263–267. <https://doi.org/10.1038/nclimate3240>, 2017.
- Brodzik, M. J., & Knowles, K. W.: Chapter 5: EASE-grid: A versatile set of equal-area projections and grids. In M. F. Goodchild (Ed.), *Discrete global grids: A web book* (pp. 98–113). Santa Barbara, CA: National Center for Geographic Information & Analysis. Retrieved from <https://escholarship.org/uc/item/9492q6sm>, 2002.
- Chen, W.-N., Chiang, C.-W., & Nee, J.-B.: Lidar ratio and depolarization ratio for cirrus clouds. *Applied Optics*, 41(30), 6470. <https://doi.org/10.1364/AO.41.006470>, 2002.
- Chung, Y.-C., Bélair, S., & Mailhot, J.: Blowing Snow on Arctic Sea Ice: Results from an Improved Sea Ice–Snow–Blowing Snow Coupled System. *Journal of Hydrometeorology*, 12(4), 678–689. <https://doi.org/10.1175/2011JHM1293.1>, 2011.
- Clancy, R., Bitz, C. M., Blanchard-Wrigglesworth, E., McGraw, M. C., & Cavallo, S. M.: A cyclone-centered perspective on the drivers of asymmetric patterns in the atmosphere and sea ice during Arctic cyclones. *Journal of Climate*, 1–47. <https://doi.org/10.1175/JCLI-D-21-0093.1>, 2022.
- Dai, A.: Temperature and pressure dependence of the rain-snow phase transition over land and ocean. *Geophysical Research Letters*, 35(12). <https://doi.org/10.1029/2008gl033295>, 2008.

822 Déry, S. J., & Tremblay, L.-B.: Modeling the Effects of Wind Redistribution on the Snow Mass Budget of Polar Sea
823 Ice. *Journal of Physical Oceanography*, 34(1), 258–271. [https://doi.org/10.1175/1520-](https://doi.org/10.1175/1520-0485(2004)034<0258:MTEOWR>2.0.CO;2)
824 0485(2004)034<0258:MTEOWR>2.0.CO;2, 2004.

825 Déry, S. J., & Yau, M. K.: A Bulk Blowing Snow Model. *Boundary-Layer Meteorology*, 93(2), 237–251.
826 <https://doi.org/10.1023/A:1002065615856>, 1999.

827 Déry, S. J., & Yau, M. K.: Simulation Of Blowing Snow In The Canadian Arctic Using A Double-Moment Model.
828 *Boundary-Layer Meteorology*, 99(2), 297–316. <https://doi.org/10.1023/A:1018965008049>, 2001.

829 Déry, S. J., & Yau, M. K.: Large-scale mass balance effects of blowing snow and surface sublimation. *Journal of*
830 *Geophysical Research: Atmospheres*, 107(D23). <https://doi.org/10.1029/2001JD001251>, 2002.

831 Frey, M. M., Norris, S. J., Brooks, I. M., Anderson, P. S., Nishimura, K., Yang, X., Jones, A. E., Nerentorp
832 Mastromonaco, M. G., Jones, D. H., & Wolff, E. W.: First direct observation of sea salt aerosol production from
833 blowing snow above sea ice. *Atmospheric Chemistry and Physics*, 20(4), 2549–2578. [https://doi.org/10.5194/acp-](https://doi.org/10.5194/acp-20-2549-2020)
834 20-2549-2020, 2020.

835 Gallée, H., Guyomarc’h, G., & Brun, E.: Impact Of Snow Drift On The Antarctic Ice Sheet Surface Mass Balance:
836 Possible Sensitivity To Snow-Surface Properties. *Boundary-Layer Meteorology*, 99(1), 1–19.
837 <https://doi.org/10.1023/A:1018776422809>, 2001.

838 Gallée, H., Trouvilliez, A., Agosta, C., Genthon, C., Favier, V., & Naaim-Bouvet, F.: Transport of Snow by the
839 Wind: A Comparison Between Observations in Adélie Land, Antarctica, and Simulations Made with the Regional
840 Climate Model MAR. *Boundary-Layer Meteorology*, 146(1), 133–147. <https://doi.org/10.1007/s10546-012-9764-z>,
841 2013.

842 Gelaro, R., McCarty, W., Suárez, M. J., Todling, R., Molod, A., Takacs, L., Randles, C. A., Darmenov, A.,
843 Bosilovich, M. G., Reichle, R., Wargan, K., Coy, L., Cullather, R., Draper, C., Akella, S., Buchard, V., Conaty, A.,
844 da Silva, A. M., Gu, W., ... Zhao, B.: The Modern-Era Retrospective Analysis for Research and Applications,
845 Version 2 (MERRA-2). *Journal of Climate*, 30(14), 5419–5454. <https://doi.org/10.1175/JCLI-D-16-0758.1>, 2017.

846 Gong, X., Zhang, J., Croft, B., Yang, X., Frey, M. M., Bergner, N., Chang, R. Y.-W., Creamean, J. M., Kuang, C.,
847 Martin, R. V., Ranjithkumar, A., Sedlacek, A. J., Uin, J., Willmes, S., Zawadowicz, M. A., Pierce, J. R., Shupe, M.
848 D., Schmale, J., & Wang, J.: Arctic warming by abundant fine sea salt aerosols from blowing snow. *Nature*
849 *Geoscience*, 16(9), 768–774. <https://doi.org/10.1038/s41561-023-01254-8>, 2023.

850 Herzfeld, U., Hayes, A., Palm, S., Hancock, D., Vaughan, M., & Barbieri, K.: Detection and Height Measurement of
851 Tenuous Clouds and Blowing Snow in ICESat-2 ATLAS Data. *Geophysical Research Letters*, 48(17),
852 e2021GL093473. <https://doi.org/10.1029/2021GL093473>, 2021.

853 Hofer, S., Amory, C., Kittel, C., Carlsen, T., Le Toumelin, L., & Storelvmo, T.: The Contribution of Drifting Snow
854 to Cloud Properties and the Atmospheric Radiative Budget Over Antarctica. *Geophysical Research Letters*, 48(22).
855 <https://doi.org/10.1029/2021gl094967>, 2021.

856 Huang, J., & Jaeglé, L.: Wintertime enhancements of sea salt aerosol in polar regions consistent with a sea ice
857 source from blowing snow. *Atmospheric Chemistry and Physics*, 17(5), 3699–3712. [https://doi.org/10.5194/acp-17-](https://doi.org/10.5194/acp-17-3699-2017)
858 3699-2017, 2017.

859 Huang, J., Jaeglé, L., Chen, Q., Alexander, B., Sherwen, T., Evans, M. J., Theys, N., & Choi, S.: Evaluating the
860 impact of blowing-snow sea salt aerosol on springtime BrO and O₃ in the Arctic. *Atmospheric Chemistry and*
861 *Physics*, 20(12), 7335–7358. <https://doi.org/10.5194/acp-20-7335-2020>, 2020.

862 Huang, N., Bao, J., Yu, H., and Li, G.: Snow particle fragmentation enhances snow sublimation, *Atmospheric*
863 *Chemistry and Physics*, 25, 12535–12548, <https://doi.org/10.5194/acp-25-12535-2025>, 2025.

864 Intrieri, J. M., & Shupe, M. D.: Characteristics and Radiative Effects of Diamond Dust over the Western Arctic
865 Ocean Region. *Journal of Climate*, 17(15), 2953–2960. [https://doi.org/10.1175/1520-](https://doi.org/10.1175/1520-0442(2004)017<2953:CAREOD>2.0.CO;2)
866 0442(2004)017<2953:CAREOD>2.0.CO;2, 2004.

867 Jonassen, M. O., Välisuo, I., Vihma, T., Uotila, P., Makshtas, A. P., & Launiainen, J.: Assessment of Atmospheric
868 Reanalyses With Independent Observations in the Weddell Sea, the Antarctic. *Journal of Geophysical Research:*
869 *Atmospheres*, 124(23), 12468–12484. <https://doi.org/10.1029/2019jd030897>, 2019.

870 Josset, D., Pelon, J., Garnier, A., Hu, Y., Vaughan, M., Zhai, P., Kuehn, R., & Lucker, P.: Cirrus optical depth and
871 lidar ratio retrieval from combined CALIPSO-CloudSat observations using ocean surface echo. *Journal of*
872 *Geophysical Research: Atmospheres*, 117(D5), 2011JD016959. <https://doi.org/10.1029/2011JD016959>, 2012.

873 Kenigson, J. S., & Timmermans, M.-L.: Arctic Cyclone Activity and the Beaufort High. *Journal of Climate*, 34(10),
874 4119–4127. <https://doi.org/10.1175/jcli-d-20-0771.1>, 2021.

875 King, J. C., Anderson, P. S., Vaughan, D. G., Mann, G. W., Mobbs, S. D., & Vosper, S. B.: Wind-borne
876 redistribution of snow across an Antarctic ice rise. *Journal of Geophysical Research: Atmospheres*, 109(D11),
877 2003JD004361. <https://doi.org/10.1029/2003JD004361>, 2004.

878 Krnavek, L., Simpson, W. R., Carlson, D., Domine, F., Douglas, T. A., & Sturm, M.: The chemical composition of
879 surface snow in the Arctic: Examining marine, terrestrial, and atmospheric influences. *Atmospheric Environment*,
880 50, 349–359. <https://doi.org/10.1016/j.atmosenv.2011.11.033>, 2012.

881 Kwok, R., & Untersteiner, N.: The thinning of Arctic sea ice. *Physics Today*, 64(4), 36–41.
882 <https://doi.org/10.1063/1.3580491>, 2011.

883 Lecomte, O., Fichet, T., Flocco, D., Schroeder, D., & Vancoppenolle, M.: Interactions between wind-blown snow
884 redistribution and melt ponds in a coupled ocean–sea ice model. *Ocean Modelling*, 87, 67–80.
885 <https://doi.org/10.1016/j.ocemod.2014.12.003>, 2015.

886 Lenaerts, J. T. M., Van Den Broeke, M. R., Déry, S. J., König-Langlo, G., Ettema, J., & Munneke, P. K.: Modelling
887 snowdrift sublimation on an Antarctic ice shelf. *The Cryosphere*, 4(2), 179–190. [https://doi.org/10.5194/tc-4-179-](https://doi.org/10.5194/tc-4-179-2010)
888 2010, 2010.

889 Lenaerts, J. T. M., Van Den Broeke, M. R., Van Angelen, J. H., Van Meijgaard, E., & Déry, S. J.: Drifting snow
890 climate of the Greenland ice sheet: A study with a regional climate model. *The Cryosphere*, 6(4), 891–899.
891 <https://doi.org/10.5194/tc-6-891-2012>, 2012.

892 Lesins, G., Bourdages, L., Duck, T. J., Drummond, J. R., Eloranta, E. W., & Walden, V. P.: Large surface radiative
893 forcing from topographic blowing snow residuals measured in the High Arctic at Eureka. *Atmospheric Chemistry*
894 *and Physics*, 9(6), 1847–1862. <https://doi.org/10.5194/acp-9-1847-2009>, 2009.

895 Li, L., & Pomeroy, J. W. (1997a). Estimates of Threshold Wind Speeds for Snow Transport Using Meteorological
896 Data. *Journal of Applied Meteorology*, 36(3), 205–213. [https://doi.org/10.1175/1520-](https://doi.org/10.1175/1520-0450(1997)036<0205:EOTWSF>2.0.CO;2)
897 0450(1997)036<0205:EOTWSF>2.0.CO;2

898 Li, L., & Pomeroy, J. W. (1997b). Probability of occurrence of blowing snow. *Journal of Geophysical Research:*
899 *Atmospheres*, 102(D18), 21955–21964. <https://doi.org/10.1029/97JD01522>

900 Li, Q., Luo, Y., Yang, X., Zilker, B., Richter, A., Dou, K., Zhou, H., Zhan, K., Si, F., and Liu, W.: Tropospheric
901 bromine monoxide in Ny-Ålesund: source analysis and impacts on atmospheric chemistry, *EGUsphere* [preprint],
902 <https://doi.org/10.5194/egusphere-2025-4601>, 2025.

903 Liston, G. E., & Elder, K.: A Meteorological Distribution System for High-Resolution Terrestrial Modeling
904 (MicroMet). *Journal of Hydrometeorology*, 7(2), 217–234. <https://doi.org/10.1175/jhm486.1>, 2006.

905 Liston, G. E., Haehnel, R. B., Sturm, M., Hiemstra, C. A., Berezovskaya, S., & Tabler, R. D.: Simulating complex
906 snow distributions in windy environments using SnowTran-3D. *Journal of Glaciology*, 53(181), 241–256.
907 <https://doi.org/10.3189/172756507782202865>, 2007.

908 Liston, G. E., Itkin, P., Stroeve, J., Tschudi, M., Stewart, J. S., Pedersen, S. H., Reinking, A. K., & Elder, K.: A
909 Lagrangian Snow-Evolution System for Sea-Ice Applications (SnowModel-LG): Part I—Model Description. *Journal*
910 *of Geophysical Research: Oceans*, 125(10). <https://doi.org/10.1029/2019JC015913>, 2020.

911 Liston, G. E., Polashenski, C., Rösel, A., Itkin, P., King, J., Merkouriadi, I., & Haapala, J.: A Distributed Snow-
912 Evolution Model for Sea-Ice Applications (SnowModel). *Journal of Geophysical Research: Oceans*, 123(5), 3786–
913 3810. <https://doi.org/10.1002/2017JC013706>, 2018.

914 Liston, G. E., & Sturm, M.: A snow-transport model for complex terrain. *Journal of Glaciology*, 44(148), 498–516.
915 <https://doi.org/10.3189/S0022143000002021>, 1998.

916 Liston, G. E., & Sturm, M.: The role of winter sublimation in the Arctic moisture budget. *Hydrology Research*,
917 35(4–5), 325–334. <https://doi.org/10.2166/nh.2004.0024>, 2004.

918 Luo, L., Zhang, J., Hock, R., & Yao, Y.: Case Study of Blowing Snow Impacts on the Antarctic Peninsula Lower
919 Atmosphere and Surface Simulated With a Snow/Ice Enhanced WRF Model. *Journal of Geophysical Research:*
920 *Atmospheres*, 126(2). <https://doi.org/10.1029/2020jd033936>, 2021.

921 Mann, G. W., Anderson, P. S., & Mobbs, S. D.: Profile measurements of blowing snow at Halley, Antarctica.
922 *Journal of Geophysical Research: Atmospheres*, 105(D19), 24491–24508. <https://doi.org/10.1029/2000JD900247>,
923 2000.

924 Markus, T., Neumann, T., Martino, A., Abdalati, W., Brunt, K., Csatho, B., Farrell, S., Fricker, H., Gardner, A.,
925 Harding, D., Jasinski, M., Kwok, R., Magruder, L., Lubin, D., Luthcke, S., Morison, J., Nelson, R.,
926 Neuenschwander, A., Palm, S., ... Zwally, J.: The Ice, Cloud, and land Elevation Satellite-2 (ICESat-2): Science
927 requirements, concept, and implementation. *Remote Sensing of Environment*, 190, 260–273.
928 <https://doi.org/10.1016/j.rse.2016.12.029>, 2017.

929 Marshall, G. J., Kivinen, S., Jylhä, K., Vignols, R. M., & Rees, W. G.: The accuracy of climate variability and trends
930 across Arctic Fennoscandia in four reanalyses. *International Journal of Climatology*, 38(10), 3878–3895.
931 <https://doi.org/10.1002/joc.5541>, 2018.

932 McCrystall, M. R., Stroeve, J., Serreze, M., Forbes, B. C., & Screen, J. A.: New climate models reveal faster and
933 larger increases in Arctic precipitation than previously projected. *Nature Communications*, 12(1), 6765.
934 <https://doi.org/10.1038/s41467-021-27031-y>, 2021.

935 Merkouriadi, I., Cheng, B., Graham, R. M., Rösel, A., & Granskog, M. A.: Critical Role of Snow on Sea Ice Growth
936 in the Atlantic Sector of the Arctic Ocean. *Geophysical Research Letters*, 44(20).
937 <https://doi.org/10.1002/2017gl075494>, 2017.

938 Merkouriadi, I., Gallet, J., Graham, R. M., Liston, G. E., Polashenski, C., Rösel, A., & Gerland, S.: Winter snow
939 conditions on Arctic sea ice north of Svalbard during the Norwegian young sea ICE (N-ICE2015) expedition.
940 *Journal of Geophysical Research: Atmospheres*, 122(20). <https://doi.org/10.1002/2017jd026753>, 2017.

941 Neumann, T. A., Martino, A. J., Markus, T., Bae, S., Bock, M. R., Brenner, A. C., Brunt, K. M., Cavanaugh, J.,
942 Fernandes, S. T., Hancock, D. W., Harbeck, K., Lee, J., Kurtz, N. T., Luers, P. J., Luthcke, S. B., Magruder, L.,
943 Pennington, T. A., Ramos-Izquierdo, L., Rebold, T., ... Thomas, T. C.: The Ice, Cloud, and Land Elevation Satellite
944 – 2 mission: A global geolocated photon product derived from the Advanced Topographic Laser Altimeter System.
945 *Remote Sensing of Environment*, 233, 111325. <https://doi.org/10.1016/j.rse.2019.111325>, 2019.

946 Nishimura, K., & Nemoto, M.: Blowing snow at Mizuho station, Antarctica. *Philosophical Transactions of the*
947 *Royal Society A: Mathematical, Physical and Engineering Sciences*, 363(1832), 1647–1662.
948 <https://doi.org/10.1098/rsta.2005.1599>, 2005.

949 Palm, S. P., Kayetha, V., & Yang, Y.: Toward a Satellite-Derived Climatology of Blowing Snow Over Antarctica.
950 *Journal of Geophysical Research: Atmospheres*, 123(18). <https://doi.org/10.1029/2018JD028632>, 2018.

951 Palm, S. P., Kayetha, V., Yang, Y., & Pauly, R.: Blowing snow sublimation and transport over Antarctica from 11
952 years of CALIPSO observations. *The Cryosphere*, 11(6), 2555–2569. <https://doi.org/10.5194/tc-11-2555-2017>,
953 2017.

954 Palm, S. P., Y. Yang, U. C. Herzfeld, D. Hancock, K. A. Barbieri, J. Wimert, & the ICESat-2 Science Team.:
955 ATLAS/ICESat-2 L3A Calibrated Backscatter Profiles and Atmospheric Layer Characteristics, Version 6 [Dataset].
956 NASA National Snow and Ice Data Center Distributed Active Archive Center.
957 <https://doi.org/10.5067/ATLAS/ATL09.006>, 2023.

958 Palm, S. P., Yang, Y., Herzfeld, U., Hancock, D., Hayes, A., Selmer, P., Hart, W., & Hlavka, D.: ICESat-2
959 Atmospheric Channel Description, Data Processing and First Results. *Earth and Space Science*, 8(8),
960 e2020EA001470. <https://doi.org/10.1029/2020EA001470>, 2021.

961 Palm, S. P., Yang, Y., Kayetha, V., & Nicolas, J. P.: Insight into the Thermodynamic Structure of Blowing-Snow
962 Layers in Antarctica from Dropsonde and CALIPSO Measurements. *Journal of Applied Meteorology and*
963 *Climatology*, 57(12), 2733–2748. <https://doi.org/10.1175/JAMC-D-18-0082.1>, 2018.

964 Palm, S. P., Yang, Y., Spinhirne, J. D., & Marshak, A.: Satellite remote sensing of blowing snow properties over
965 Antarctica. *Journal of Geophysical Research*, 116(D16), D16123. <https://doi.org/10.1029/2011JD015828>, 2011.

966 Palm, S. P., Yang, Y., Hertzfeld, U., & Hancock, D.: Ice, Cloud, and Land Elevation Satellite (ICESat-2) Project
967 Algorithm Theoretical Basis Document for the Atmosphere, Part I: Level 2 and 3 Data Products, version 6.
968 <https://doi.org/10.5067/H975R4YYVIT6>, 2022.

969 Pomeroy, J. W., Marsh, P., & Gray, D. M.: Application of a distributed blowing snow model to the Arctic.
970 *Hydrological Processes*, 11(11), 1451–1464. [https://doi.org/10.1002/\(SICI\)1099-1085\(199709\)11:11<1451::AID-
971 HYP449>3.0.CO;2-Q](https://doi.org/10.1002/(SICI)1099-1085(199709)11:11<1451::AID-HYP449>3.0.CO;2-Q), 1997.

972 Ranjithkumar, A., Duncan, E., Yang, X., Partridge, D. G., Lachlan-Cope, T., Gong, X., Nishimura, K., & Frey, M.
973 M.: Direct observation of Arctic Sea salt aerosol production from blowing snow and modeling over a changing sea
974 ice environment. *Elem Sci Anth*, 13(1). <https://doi.org/10.1525/elementa.2024.00006>, 2025.

975 Rantanen, M., Karpechko, A. Yu., Lipponen, A., Nordling, K., Hyvärinen, O., Ruosteenoja, K., Vihma, T., &
976 Laaksonen, A.: The Arctic has warmed nearly four times faster than the globe since 1979. *Communications Earth &
977 Environment*, 3(1), 168. <https://doi.org/10.1038/s43247-022-00498-3>, 2022.

978 Rhodes, R. H., Yang, X., Wolff, E. W., McConnell, J. R., & Frey, M. M.: Sea ice as a source of sea salt aerosol to
979 Greenland ice cores: A model-based study. *Atmospheric Chemistry and Physics*, 17(15), 9417–9433.
980 <https://doi.org/10.5194/acp-17-9417-2017>, 2017.

981 Rinke, A., Cassano, J. J., Cassano, E. N., Jaiser, R., & Handorf, D.: Meteorological conditions during the MOSAiC
982 expedition. *Elementa: Science of the Anthropocene*, 9(1), 00023. <https://doi.org/10.1525/elementa.2021.00023>,
983 2021.

984 Robinson, J., Jaeglé, L., Palm, S. P., Shupe, M. D., Liston, G. E., & Frey, M. M.: ICESat-2 observations of blowing
985 snow over Arctic sea ice during the 2019–2020 MOSAiC expedition. *Journal of Geophysical Research:
986 Atmospheres*, 130, e2025JD043919. <https://doi.org/10.1029/2025JD043919>, 2025.

987 Schmidt, R. A.: Vertical profiles of wind speed, snow concentration, and humidity in blowing snow. *Boundary-
988 Layer Meteorology*, 23(2), 223–246. <https://doi.org/10.1007/BF00123299>, 1982.

989 Serreze, M. C., & Barrett, A. P.: Characteristics of the Beaufort Sea High. *Journal of Climate*, 24(1), 159–182.
990 <https://doi.org/10.1175/2010jcli3636.1>, 2011.

991 Shupe, M. D., Walden, V. P., Eloranta, E., Uttal, T., Campbell, J. R., Starkweather, S. M., & Shiobara, M.: Clouds
992 at Arctic Atmospheric Observatories. Part I: Occurrence and Macrophysical Properties. *Journal of Applied
993 Meteorology and Climatology*, 50(3), 626–644. <https://doi.org/10.1175/2010JAMC2467.1>, 2011.

994 Stroeve, J., & Notz, D.: Changing state of Arctic sea ice across all seasons. *Environmental Research Letters*, 13(10),
995 103001. <https://doi.org/10.1088/1748-9326/aade56>, 2018.

996 Sturm, M., Holmgren, J., & Perovich, D. K.: Winter snow cover on the sea ice of the Arctic Ocean at the Surface
997 Heat Budget of the Arctic Ocean (SHEBA): Temporal evolution and spatial variability. *Journal of Geophysical
998 Research: Oceans*, 107(C10). <https://doi.org/10.1029/2000jc000400>, 2002.

999 Tschudi, M. A., Meier, W. N., & Stewart, J. S.: An enhancement to sea ice motion and age products at the National
1000 Snow and Ice Data Center (NSIDC). *The Cryosphere*, 14(5), 1519–1536. <https://doi.org/10.5194/tc-14-1519-2020>,
1001 2020.

1002 Tschudi, M. & Univ Of CO.: Polar Pathfinder Daily 25 km EASE-Grid Sea Ice Motion Vectors [Dataset]. NASA
1003 National Snow and Ice Data Center Distributed Active Archive Center. <https://doi.org/10.5067/INAWUWO7QH7B>,
1004 2019.

1005 Valkonen, E., Cassano, J., & Cassano, E.: Arctic Cyclones and Their Interactions With the Declining Sea Ice: A
1006 Recent Climatology. *Journal of Geophysical Research: Atmospheres*, 126(12).
1007 <https://doi.org/10.1029/2020jd034366>, 2021.

1008 Webster, M., Gerland, S., Holland, M., Hunke, E., Kwok, R., Lecomte, O., Massom, R., Perovich, D., & Sturm, M.:
1009 Snow in the changing sea-ice systems. *Nature Climate Change*, 8(11), 946–953. [https://doi.org/10.1038/s41558-018-
1010 0286-7](https://doi.org/10.1038/s41558-018-0286-7), 2018.

1011 Winker, D. M., Vaughan, M. A., Omar, A., Hu, Y., Powell, K. A., Liu, Z., Hunt, W. H., & Young, S. A.: Overview
1012 of the CALIPSO Mission and CALIOP Data Processing Algorithms. *Journal of Atmospheric and Oceanic
1013 Technology*, 26(11), 2310–2323. <https://doi.org/10.1175/2009JTECHA1281.1>, 2009.

1014 Yang, J., & Yau, M. K.: A New Triple-Moment Blowing Snow Model. *Boundary-Layer Meteorology*, 126(1), 137–
1015 155. <https://doi.org/10.1007/s10546-007-9215-4>, 2007.

1016 Yang, J., Yau, M. K., Fang, X., & Pomeroy, J. W.: A triple-moment blowing snow-atmospheric model and its
1017 application in computing the seasonal wintertime snow mass budget. *Hydrology and Earth System Sciences*, 14(6),
1018 1063–1079. <https://doi.org/10.5194/hess-14-1063-2010>, 2010.

1019 Yang, X., Frey, M. M., Rhodes, R. H., Norris, S. J., Brooks, I. M., Anderson, P. S., Nishimura, K., Jones, A. E., &
1020 Wolff, E. W.: Sea salt aerosol production via sublimating wind-blown saline snow particles over sea ice:
1021 Parameterizations and relevant microphysical mechanisms. *Atmospheric Chemistry and Physics*, 19(13), 8407–
1022 8424. <https://doi.org/10.5194/acp-19-8407-2019>, 2019.

1023 Yang, X., Pyle, J. A., & Cox, R. A.: Sea salt aerosol production and bromine release: Role of snow on sea ice.
1024 *Geophysical Research Letters*, 35(16), L16815. <https://doi.org/10.1029/2008GL034536>, 2008.

1025 Yang, Y., Palm, S. P., Marshak, A., Wu, D. L., Yu, H., & Fu, Q.: First satellite-detected perturbations of outgoing
1026 longwave radiation associated with blowing snow events over Antarctica. *Geophysical Research Letters*, 41(2),
1027 730–735. <https://doi.org/10.1002/2013GL058932>, 2014.

1028 Zhang, D., Vogelmann, A., Kollias, P., Luke, E., Yang, F., Lubin, D., & Wang, Z.: Comparison of Antarctic and
1029 Arctic Single-Layer Stratiform Mixed-Phase Cloud Properties Using Ground-Based Remote Sensing Measurements.
1030 *Journal of Geophysical Research: Atmospheres*, 124(17–18), 10186–10204. <https://doi.org/10.1029/2019JD030673>,
1031 2019.